RDU150325

TAILORING THE ELECTROCHEMICAL PROPERTIESOF TITANIUM DIOXIDE FOR HIGH PERFORMANCE ENERGY STORAGE DEVICE

JOSE RAJAN

IZAN IZWAN MISNON

JAMIL ISMAIL

RESEARCH VOTE NO: RDU150325

FACULTY OF INDUSTRIAL SCIENCES AND TECHNOLOGY

UNIVERSITI MALAYSIA PAHANG

2016

Abstract

Supercapacitors are emerging as a desirable energy storage medium in view of their order of magnitude higher power density than batteries and energy density than electronic capacitors. One of the key issues in the development of a suitable electrode material for supercapacitors is that materials showing large specific capacitance are poorly abundant. In this research, we show that niobium doped titanium dioxide (Nb:TiO_2) and nickel doped titanium dioxide (Ni:TiO_2) nanowires developed by electrospinning have an order of magnitude higher capacitance (~280 Fg^{-1}) than pristine TiO_2 (~40 Fg^{-1}) or zirconium doped TiO_2 (~30 Fg^{-1}) nanowires. The cyclic voltammetry and charge discharge cycling experiments show that the Nb:TiO_2 nanowires have 100% coulombic efficiency and could be operated over 5000 cycles without any appreciable capacitance degradation. The superior charge storage capability of the Nb:TiO_2 is assigned to its high electrical conductivity as determined by electrochemical impedance spectroscopy. A practical supercapacitor is fabricated in asymmetric configuration using the Nb:TiO_2 as anode and activated carbon as cathode. The device delivered energy densities of 16.3, 11.4 and 5.6 $Whkg^{-1}$ at power densities of 770, 1310, and 1900 Wkg^{-1}, respectively. These values are much superior than a control device fabricated using activated carbon as its both electrodes.

Keywords: Asymmetric Supercapacitor, Ceramic nanostructures, Renewable energy, Batteries, TiO_2 nanostructures, One-dimensional nanostructures.

TABLE OF CONTENET

CHAPTER I

GENERAL INTRODUCTION

1.1 Introduction

A fast-growing market for portable electronic devices and hybrid electric vehicles(HEVs) has led to intense research in the area of electrical energy storage devices characterized by high energy densities (100–200 W h kg^{-1}), power densities (5 kW kg^{-1}) and a long cycle life (10^5 cycles). Supercapacitors represent a unique class of energy storage devices including electric double layer capacitors, pseudocapacitors, and hybrid capacitors; recent review articles on this topic may be found elsewhere.[1-6] Electric double layer capacitors (EDLCs) store electrical energy via the accumulation of electric charges at an electrical double layer formed at the interface between a mesoporous electrode and an electrolyte. Carbon structures such as activated carbon, carbon nanotubes, and graphene have been chosen to build EDLCs. No electron transfer takes place across the electrode–electrolyte interface during its operation and therefore this charge storage process is non-faradic.[7, 8] Pseudocapacitors involve faradic charge storage processes facilitated by a redox reaction at the electrode–electrolyte interface.[9, 10] Transition metal oxides (TMOs) and conducting polymers show high pseudocapacitance; a theoretical pseudocapacitance equal to F/(ΔE ×m), where F is the Faraday constant, m is the molecular weight and ΔE is the redox potential of the material, could be achieved by TMOs.[11] A high specific surface area of the electrode material to enable a large electrode–electrolyte interface for efficient redox reaction, high electrical conductivity to enable high rate charging and discharging, and faster ion diffusivity are properties of

TMOs and electrolytes required to achieve higher energy and power densities in pseudocapacitors.

Transition metal oxides (TMOs) are promising pseudo-capacitance candidates due to availability of multiple oxidation states[12]. Popular TMOs include RuO_2, MnO_2, NiO,V_2O_5 and Co_3O_4 due to their high specific capacitance and electrochemical reversibility [13]. As 1D morphologies offer directed charge transport they have high electrical conductivities. Moreover, increased surface area of low diameter nanowires helps in maximum utilisation of active electrode materials. Various chemical methods are utilised to synthesize 1D morphologies of supercapacitor electrode material [13]. However, compared with other processes adopted, electrospinning is a simple, versatile and cost-effective method to produce low diameter 1D nanostructures.

1.2 Problem statement

TMOs such as nickel oxide, copper oxide, manganese dioxide and ruthenium oxide are commonly used in the construction of supercapacitor electrodes as they excel in increasing electrical conductivity and chemical capacitance of the electrodes for use in energy storage devices. However, these TMOs present drawbacks including skin and respiratory irritant and in excess is toxic to the environment. Safe disassembling of used TMO containing devices for recycling purposes is difficult due to its irritancy. Irresponsibly discarded devices causes leaching of TMOs to the environment which is destructive to marine life and plants. Moreover, these TMOs are less-abundant in the earth's crust, which impart constraints in terms of supply and cost of raw materials. In order to solve the problem, an electrode composed of less toxic and environmentally friendly material is required.

1.3 Objectives

i. Identifying the controlling factors affecting the electrochemical properties of titanium dioxide.

ii. Developing an asymmetric supercapacitor device and evaluation of their energy and power density.

1.4 Scope of the research

This study is limited to doping TiO_2 with transition metal ions (niobium, nickel, and zirconium) in nanowire forms developed by electrospinning process. The synthesis of nanowires electrospinning requires optimization of the polymeric solution, electrospinning parameters and annealing procedures to obtain the inorganic nanowires. Next, the chemical and structural characteristics of the nanowires are to be determined to determine the source of its properties. These could be done by X-ray and electron diffraction as well as energy dispersive X-ray analysis of identifying the phase and phase purity, scanning and transmission electron microscopy for morphological aspects, and absorption spectroscopy to confirm whether doping is achieved.

The controlling factors of charge storage could be studied by cyclic voltammetry, galvanostatic charge discharge, and electrochemical impedance spectroscopy measurements. Electrodes with optimum mass loading are to be developed for this purpose. Although there are many electrolyte systems proposed, aqueous alkaline electrolytes will be used in the present project due to its wide popularity and electrical conductivity.

Practical device for this study is in the form of an asymmetric supercapacitor with one of its electrode from a battery type material and the other from the supercapacitor electrode. The ASCs were fabricated by assembling the Nb:TiO_2 nanowire (anode) and the

AC (cathode) electrodes separated by a glass microfiber filter (fioroni) in 3 M KOH. The amount of active materials for fabrication of ASC was calculated based on the charge balance between the electrodes such that the effective capacitance at each electrode is same (See Results and Discussion section for details). A symmetric EDLC comprising of AC as both electrodes was used a control device. The capacitive properties of the ASC were obtained in two-electrode configuration at room temperature using the PGSTAT M101 potentiostat-galvanostat.

1.5 Statement of contribution

Two typical high performing low cost materials were developed during this research. Two web of science indexed journal papers and one web of science conference indexed conference proceeding papers were published from this research.

1.6 Organization of the report

Starting from a brief introduction to ECs,

Chapter 1: Presents problem statement, research objectives, scope and statement of contribution of research.

Chapter 2: Reports a comprehensive review on the working principle of supercapacitor and varied choice of the electrode material used.

Chapter 3: Presents the experimental method used in this work and the working principle of the instruments used for characterization.

Chapter 4: Data and Discussion

CHAPTER II

LITERATURE REVIEW

Energy storage devices providing high energy and power density are required to meet the ever increasing demands to power hybrid electric vehicles and multifunctional portable electronic devices [14, 15, 16]. Practical energizers, such as lithium ion batteries, have high energy density (>150 $Whkg^{-1}$) but suffer from low power density (< 200 Wkg^{-1}) and short cycle life (<1000 cycles) [17]. On the other hand, conventional capacitors have three orders of magnitude higher power density (>10^5 Wkg^{-1}) but low energy density (< 5 $Whkg^{-1}$) than batteries. Electrochemical capacitors or supercapacitors (SCs), with orders of magnitude higher power density (>10 $kWkg^{-1}$) than batteries and energy density (~50 $Whkg^{-1}$) than capacitors, can bridge the gap between the batteries and conventional capacitors. The SCs are classified into electric double layer capacitors (EDLCs) and pseudocapacitors according to the charge storage mechanisms. The EDLCs store electrical energy via accumulation of electric charges at an electrical double layer formed at an interface between a porous solid electrode and an electrolyte (non-faradic). Carbons such as activated carbon, carbon nanotubes, and graphene are choices to build EDLCs; however, their lower specific capacitance (C_S ~20 – 50 μFcm^{-2}) limit their application areas. The pseudocapacitors provide several times higher C_S (10 – 100) than EDLC due to faradic charge storage process facilitated by a redox reaction at the electrode – electrolyte interface [18, 19]. Transition metal oxides (TMOs), such as MnO_2, Co_3O_4, RuO_2, and conducting polymers show high pseudocapacitance (C_P); a theoretical C_P equal to nF / ($\Delta E \times m$), where F is the Faraday constant, n is the number of electrons transferred, m is the molecular weight and ΔE is the redox potential of the material, could be achieved by these materials[20]. Although the potential window of the pseudocapacitive materials are

lower compared to that of the carbons they are employed in the SCs as one of the electrodes to enhance the energy density. Such device configuration is termed as asymmetric supercapacitors (ASCs). Even if the intense research on SCs is aimed at increasing energy density similar to that of batteries, attention is equally given at lowering fabrication costs and on materials of larger abundance.

High electrochemical reversibility, multiple oxidation states, large surface area, and high electrical conductivity are properties required for high performance SC electrodes. Among the TMOs, TiO_2 have relatively lower toxicity, larger abundance and lower cost, environmental friendly, and desirable optical, electrical and electrochemical properties [21]. It has been extensively studied for its wide application from catalysis to energy storage [22, 23]. For its application in SCs, theoretically TiO_2 could deliver specific capacitance 700 Fg^{-1}; i.e., TiO_2 nanostructures hold good promise as a desirable SC electrode. However, its practically achieved C_S is rather low thereby limiting its commercial deployability. We believe that this poor performance could be related to the inferior electrical conductivity of nanostructured TiO_2 (~10^{-5} S/cm) [24, 25]. Doping of TiO_2 with transition metals such as W^{+6}, Nb^{5+}, V^{+5}, Ce^{+4}, Zr^{+4}, Fe^{+3} and Ni^{+3} or non-metals such as H and N is considered to be one of the efficient method to improve the electrical conductivity of TiO_2 [26, 27]. The Nb doped TiO_2 (Nb:TiO_2) have three orders of magnitude higher electrical conductivity than pristine TiO_2 [24, 30] and show superior performance in electrochemical devices.

One-dimensional charge transport makes nanowires to be preferred charge storage medium. Among the many nanowire forming techniques, electrospinning is a simple and versatile technique for continuous nanofibers and nanowires for many applications such as filtration, healthcare, and energy [31]. In the electrospinning technique, a polymeric solution, usually prepared in organic solvents, is injected through a syringe needle in the

presence of an electric field. A polymeric jet is initiated upon injection of the solution that undergoes asymmetric bending during the passage between the injector and the collector. This asymmetric bending increases the path length of the jet and allows the solvent to evaporate thereby producing solid continuous fibers with diameters ranging from nanometers to sub-micrometers on a collector surface. If the polymeric solution contains precursors for forming an inorganic solid, then appropriate annealing produces its continuous nanofibers.

In this work, we show that electrospun Nb:TiO_2 and Ni:TiO_2 nanowire electrodes display an order of magnitude higher specific capacitance (~280 Fg^{-1} and ~200 Fg^{-1} respectivly) and superior electrochemical reversibility (100% at the end of 5000 cycles) in 3 M KOH electrolyte than pristine TiO_2 or Zr:TiO_2. A working SC in asymmetric configuration was fabricated using Nb:TiO_2 as anode and commercial activated carbon as cathode which gaves the highest energy density (E_S) that employed TiO_2 nanostructures. The performance of the asymmetric supercapacitor (ASC) is four times higher than a control device, which is a symmetric EDLC fabricated using activated carbon (AC). The ASC could be cycled over 5000 times in the voltage window 0-1.5 V with no appreciable capacitance lose. Our results demonstrate that the electrospun Nb:TiO_2 and Ni:TiO_2 nanowires could be a choice of SC electrode material characterized by high C_S and related properties.

Table 2: Summary of research describing the electrochemical properties of TiO_2 electrode

Morphology	Method of synthesis	C_S (Fg^{-1})	C_S Retention(%)/Cycle number	Scan rate/ Current density	Electrolyte	Ref
TiO_2-B nanotubes	Solvothermal reaction	17.7	NR	NR	NR	33
TiO_2 nanotubes	Anodisation	911 μFcm^{-2}	NR	NR	NR	34
TiO_2 Powder	Sol-gel	181 μFcm^{-2}				34
Hydrogenated TiO_2 Nanotube	Anodic oxidation	3.24 $mFcm^{-2}$ 0.03 $mFcm^{-2}$	NR	100 mVs^{-1}	NR	35
TiO_2 nanotube array	Anodic oxidation	19.2	NR	1 mVs^{-1}	NR	49
TiO_2 particles on graphene sheet	NR	165	90/(5000)	5 mVs^{-1}	1 M Na_2SO_4	50
TiN spheres	Template free	133	NR	2 mVs^{-1}	NR	51
TiO_2 hollow nanoshells	NR	7.1 $mFcm^{-2}$	NR	NR	NR	52
RuO_2-xH_2O-TiO_2 nanoflowers	NR	425	NR	25 mVs^{-1}	NR	53
TiO_2	NR	2.6	NR	50 $mAcm^{-2}$	NR	54
TiO_2 nanotubes	Anodization	6 $mFcm^{-2}$				25
Nanoporous TiO_2	NR	NR	NR	NR	0.1 M KPF_6	55
Acivated carbon modidfied TiO_2	NR	63.1	NR	NR	NR	56
TiO_2 nanotube	anodization	3.4 $mFcm^{-2}$	NR	NR	1 M KCl	57
GNS/TiO_2 film	NR	0.86 $mFcm^{-2}$	98/(1500)	10 mVs^{-1}	0.5 M Na_2SO_4	58
RGO-$Cu_2O$$TiO_2$	NR	80	98/(1000)	0.2 Ag^{-1}	6 M KOH	59

Ti/TiO_2	NR	35.5	NR	NR	NR	60
Self assembled	NR	1.6 $mFcm^{-2}$	97/(1000)	1 mVs^{-1}	1 M NaOH	47
TiO_2@MnO_2 Nanowall arrays	NR	22.2 $mFcm^{-2}$	85/(4000)	5 mVs^{-1}	1 M Na_2SO_4	61
TiO_2 nanoparticles/ carbon nanotube	NR	145	NR	2 mVs^{-1}	NR	62
3D nanoporous H-TiO_2	NR	1.1 $mFcm^{-2}$	NR	100 mVs^{-1}	NR	63
CNT/TiO_2 nanocomposite	NR	6.9 Fg^{-1}	NR	NR	NR	64
3 D Hierarchial Co_3O_4	Solvothermal	781	98/1000	0.5 Ag^{-1}	KOH	65
Co_3O_4 nanospheres	NR	1100	85/5000	1 Ag^{-1}	6 M KOH	66
Cobalt Cobaltit nanowalls	calcination	997	93/1000	0.5 Ag^{-1}	KOH	67

NR – Not reported.

CHAPTER III

RESEARCH METHODOLOGY

The research methodology adopted is schematically shown in Figure 3.1

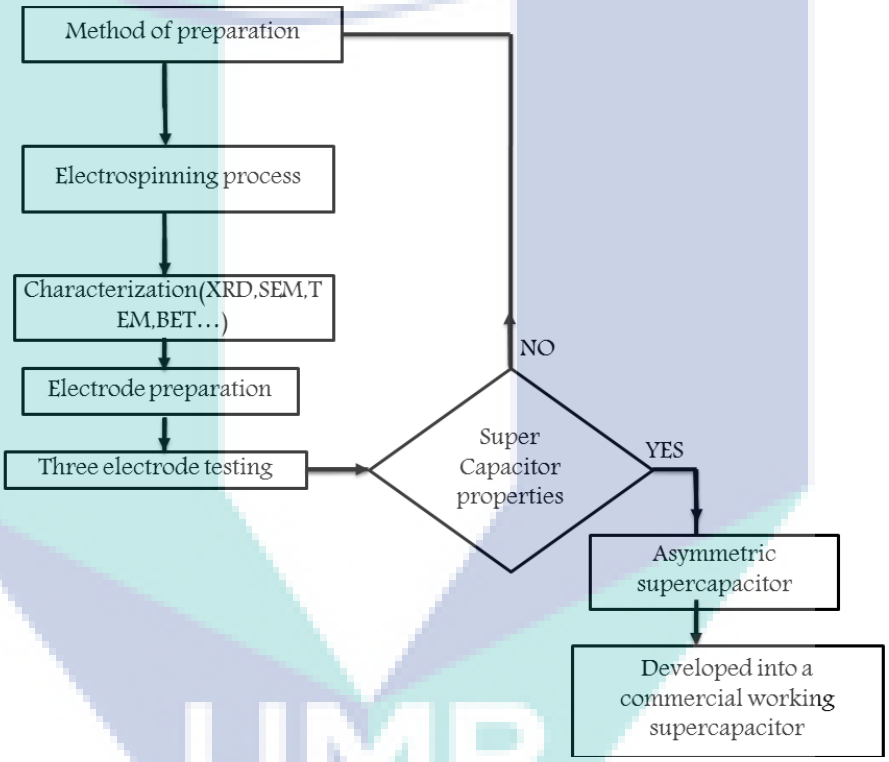

Figure 3.1: Research methodology chart

3.1 Synthesis and characterization of TiO_2, Nb:TiO_2, Ni:TiO_2 and Zr:TiO_2 nanowires

Figure(a) shows the research methodology of this project. In a typical synthesis, TiO_2, Nb:TiO_2, and Ni:TiO_2, Zr:TiO_2 nanowires were prepared by a commercial electrospinning machine (Electroris, Nanolab, Malaysia) using a previously adopted

procedure[29, 27, 32]. The niobium and nickel are doped up to 5 at.%, and zirconium up to 2at.% as the niobium doping showed improved performance than the parent material. The precursor solution for electrospinning was prepared from polyvinyl acetate (PVAc, Mw 500000), dimethyl formamide (DMF), titanium (IV) isopropoxide, niobium ethoxide (Sigma Aldrich, Singapore; 99.9%), zirconyl choloride, and acetic acid. In a typical synthesis, 4.5 g of PVAc solution in DMF (11.5 wt.%) was mixed together with titanium (IV) isopropoxide. The amounts of Ti and Nb, Ni, Zr precursors required were calculated based on the number of atoms required for replacing a given number of Ti atoms by Nb or Zr atoms. A sol was prepared by the drop wise addition of 0.5 g of acetic acid to the above solution. The resulting solution was stirred well and electrospun at 25 kV accelerating voltage and at 1 mLh^{-1} flow rate. The polymeric fibers containing Ti^{4+} and Nb^{5+}, Ni^{2+}, Zr^{4+} ions were collected on a grounded rotating drum placed at 10 cm below the spinneret.

The morphology of the as-spun and annealed nanowires were examined by scanning electron microscopy (SEM; Quanta 200 FEG System: FEI Company, Oregon) and transmission electron microscopy (TEM; JEOL 2010Fas, Tokyo,Japan). Crystal structure of the nanowires was examined by XRD (Siemens D5005, Bruker, Karlsruhe, Germany) technique. Presence of Nb and Zr in the doped materials was confirmed by X-ray fluorescence measurements employing EDX-720 (Shimadzu).

3.2 Electrode preparation and electrochemical studies

Supercapacitor electrodes were fabricated on nickel foam substrates as described before.[20] Briefly, the working electrode was prepared by mixing the nanowires with polyvinylidenefluoride (PVDF) (Sigma Aldrich, USA) and carbon black (Super P conductive, Alfa Aesar, UK) in the ratio 75:15:10. The above mixture was stirred in N-methyl-2-pyrrolidinone for better homogeneity. The as-prepared slurry was then pasted on a nickel foam substrate (area ~1 cm^2) and dried in an oven at 60 °C for 24 h. The mass

loading of active material was ~ 2.5 mgcm^{-2}. The dried electrode was then pressed using a hydraulic press at a pressure of 5 ton. Electrochemical properties of the electrodes were studied by cyclic voltammetry (CV), galvanostatic charge–discharge cycling, and electrochemical impedance spectroscopy in 3 M KOH electrolyte. These electrochemical properties in three electrode configurations were obtained at room temperature using a potentiostat galvanostat (PGSTAT M101, Metrohm Autolab B.V., Netherlands) employing NOVA 1.9 software. A platinum rod and a saturated Ag/AgCl electrode were used as the counter and the reference electrodes, respectively.

3.3 Asymmetric supercapacitor fabrication and testing

The ASCs were fabricated by assembling the Nb:TiO_2 nanowire (anode) and the AC (cathode) electrodes separated by a glass microfiber filter (fioroni) in 3 M KOH. The amount of active materials for fabrication of ASC was calculated based on the charge balance between the electrodes such that the effective capacitance at each electrode is same (See Data and Discussion section for details). A symmetric EDLC comprising of AC as both electrodes was used a control device. The capacitive properties of the ASC were obtained in two-electrode configuration at room temperature using the PGSTAT M101 potentiostat-galvanostat.

CHAPTER IV

Data & Discussion

4.1 Crystal structure and Morphology of electrospun nanowires

Fig. 1 show the crystal structures of pristine and doped TiO_2; all materials crystallized in anatase structure. The XRD peaks of the doped materials showed either a shift in the peak positions or change its profile (Inset of Fig. 1). The doping has been confirmed by chemical analysis employing X-ray fluorescence measurements. The crystallinity of the doped materials, which was judged from the *fwhm* of the XRD peaks, was appreciably different for the Nb, Ni and Zr doped analogues (Inset of Figure 1). The Zr:TiO_2 showed broader and diffused peaks than pure and Nb:TiO_2, which could be due to increased lattice strain. The lattice parameters of the materials calculated using the procedure described elsewhere from the XRD patterns are summarized in Table 1. The lattice parameters of the TiO_2 and the doped materials agree well with reported values [40, 42]. Table 1 shows that Nb decrease *a* whereas Zr decrease both *a* and *c* of the unit cell of anatase TiO_2. This difference is expected to originate from the difference in the sizes of the six-fold coordinated (which is the geometry in the anatase TiO_2) Ti^{4+} (0.605 Å), Nb^{5+} (0.64 Å), and Zr^{4+} (0.72 Å). The larger size of the six-fold coordinated Zr^{4+} ions could influence the lattice structure of anatase more than the Nb^{5+} with minor mismatch.

Table 1: Lattice parameters of pristine and doped TiO_2

Phase	Lattice parameters (Å)	
	a	c
TiO_2	3.785(3)	9.501(2)
2at.% Nb:TiO_2	3.783(7)	9.501(2)
2at.%Zr:TiO_2	3.782(5)	9.499(7)
2at.%Ni:TiO_2	3.773(3)	9.511(3)

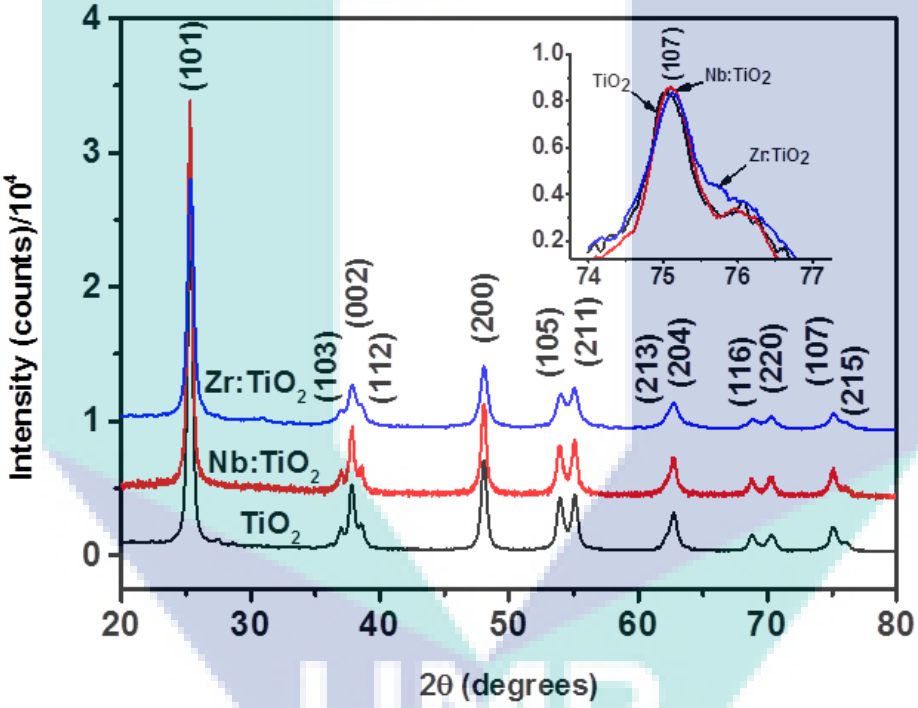

Figure 1: The XRD patterns of TiO_2, Zr: TiO_2 and Nb:TiO_2 nanowires. The inset shows the peak corresponding to the (107) plane showing a minor shift in its position.

Morphological and microstructural details of doped and undoped TiO_2 nanowires are summarised in Fig. 2. The as-spun mats showed conventional electrospun polymeric fibrous structure which upon annealing produced the targeted metal oxide structures with their diameter in the range 100 – 150 nm. The TEM images showed lowering of grain size with doping for all the dopants. The undoped TiO_2 fibres had grains of larger diameter (~

50 nm). The doped fibres were constituted by grains of lower diameter (~ 10-30 nm) implying that the doping reduced the grain growth under similar processing conditions.

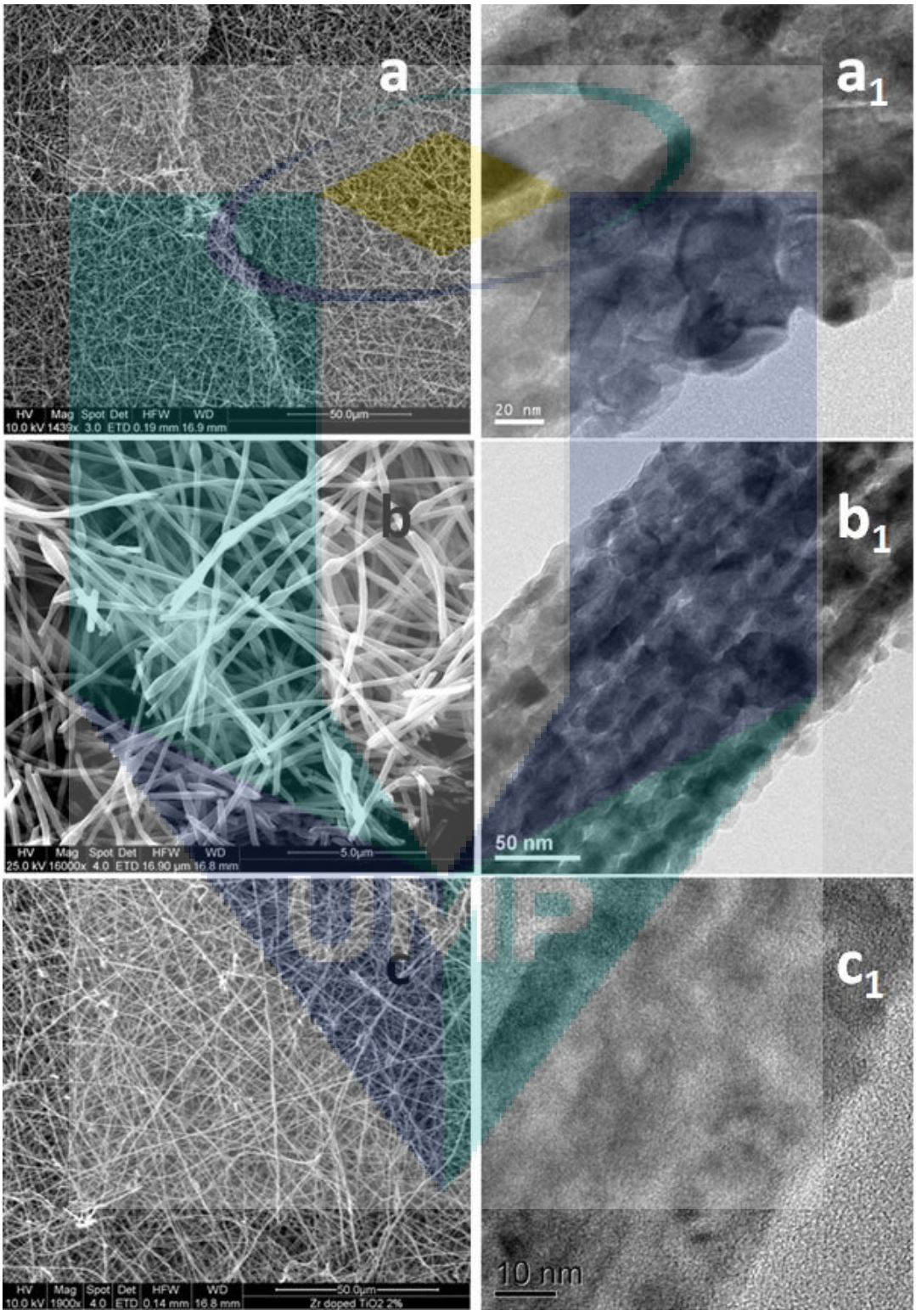

Figure 2: (a, b & c) SEM images and (a_1, b_1 & c_1) TEM images of TiO_2, Nb:TiO_2 and Zr:TiO_2 respectively

Fig. 3 summarizes the structure and morphology of the pristine and Ni:TiO_2; all materials crystallized in anatase structure with minor increase in the lattice parameters (Table 1). This increase in the lattice parameters is expected to result from the larger size of the six-fold coordinated Ni^{2+} ion (0.69 Å) compared to that of the Ti^{4+} ion for similar coordination (0.605 Å) and could be an indication that the doping has been achieved. Although the anatase phase is prominent, three weak peaks are found at respective angles representing the planes of rutile phase at 5at.% Ni:TiO_2. The EDX result shows that the content of Ni in the 2at.% Ni:TiO_2 nanowire is ~2at.%. While EDX results are semi-quantitative and not necessarily accurate, the present results showed that doping has been achieved on an average. The Ni:TiO_2 showed enhanced crystallinity as judged from the extended periodicity in the lattice image as well as from the spotty electron diffraction pattern (Figure 3 and its inset). No rutile phase was observed in the XRD pattern of 2at.%Ni:TiO_2; however, the selected area diffraction pattern detected presence of it (Inset of Figure 3). This is because XRD do not generally detect small vol.% (<0.2%) of phases; only a weak line corresponding to the rutile phase could be identified from the SAED pattern of 2at.%Ni:TiO_2. The as-spun mats showed conventional electrospun polymeric fibrous structure which upon annealing produced the oxide nanowires having diameter in the range 100 – 150 nm.

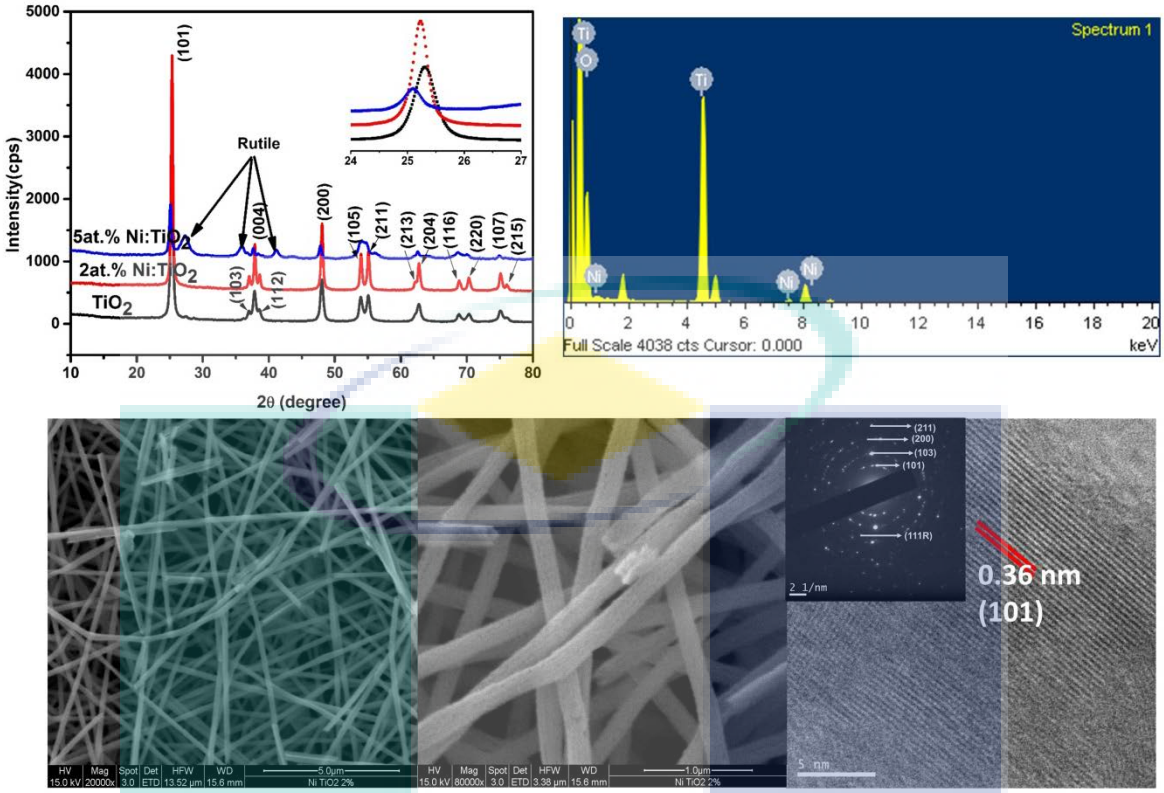

Figure 3: (a) The XRD pattern of pristine TiO_2 and Ni:TiO_2, (inset) a magnified view of the (101) plane showing the shift in the diffraction peak upon Ni doping; (b) EDX of 2 at.% Ni:TiO_2;(c&d) SEM images of 2 at.% Ni:TiO_2 at varying magnification; (e) HRTEM image of Ni:TiO_2; inset SAED of 2 at.% Ni:TiO_2

To further confirm whether doping has been achieved, changes in the absorption spectra of the doped and undoped samples have been studied. Figure 4 shows the measured diffuse reflectance spectrum (DRS) of the pure and Ni doped nanofibers (panel a) and the calculated Kubelka-Munk diagram (panel b) from it. The DRS clearly reveal the differences in the reflectance profile, and hence optical band structure, upon Ni doping. Two changes were observed in the reflectance profile upon Ni doping: (i) partial transparency in the lower energy side, indicating changes in the band structure; and (ii) a clear red shift in the absorption onset in the 5at.% doping. A change in colour of the samples from whitish-grey (pure TiO_2) to pale yellow for 5at.% Ni doping was observed,

further confirming that doping was achieved. A change in band gap of TiO_2 (~3.22 eV) was observed in the Kubelka-Munk diagram upon Ni doping although the shift was less pronounced in 2at.%Ni:TiO_2 (3.16 eV) (Figure 2b) whereas band gap of 5at.%Ni:TiO_2 significantly reduced to 2.74 eV; thereby confirming Ni doping in TiO_2.

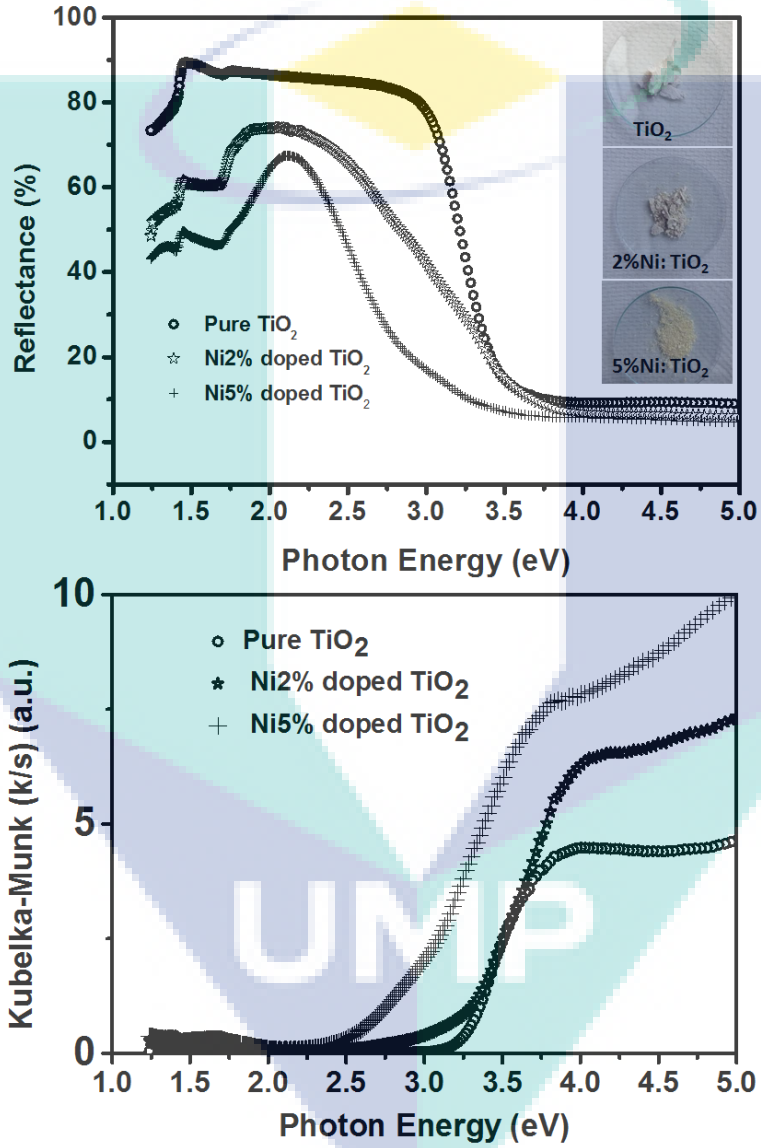

Figure 4: (a) Diffuse reflectance spectrum of pure and 2 at.% as well as 5 at.% Ni:TiO_2. Inset, photographs of (a) pure TiO_2 (b) 2 at.% Ni:TiO_2 (c) 5 at.% Ni:TiO_2. (b) Kubelka-Munk diagram calculated from the reflectance spectrum using the relation $f(R) = \frac{(1-R)^2}{2R}$, where *f(R)* is the Kubelka-Munk function and R is the reflectance.

4.2 Cyclic voltammetry

Cyclic voltammetry measurements were performed to evaluate the electrochemical behavior of the electrodes under a potential window 0 – 0.5 V. Figure 5 shows the CV curves of the electrodes of pristine TiO_2, $Zr:TiO_2$ and $Nb:TiO_2$ and $Ni:TiO_2$ measured at a scan rate 2 mVs^{-1} in 3 M KOH aqueous electrolyte. In the CV plot of the electrodes, a pair of redox peaks are seen which indicate that the origin of charge storage is reversible faradic process. These peaks can be attributed to the insertion/exertion of alkali cations into/out of the oxide nanowires with concomitant reduction/oxidation of the Ti ions, which can be expressed as

$$xK^{+} + y\,TiO_2 + e^{-} \leftrightarrow K_x(TiO_2)_y. \quad (1)$$

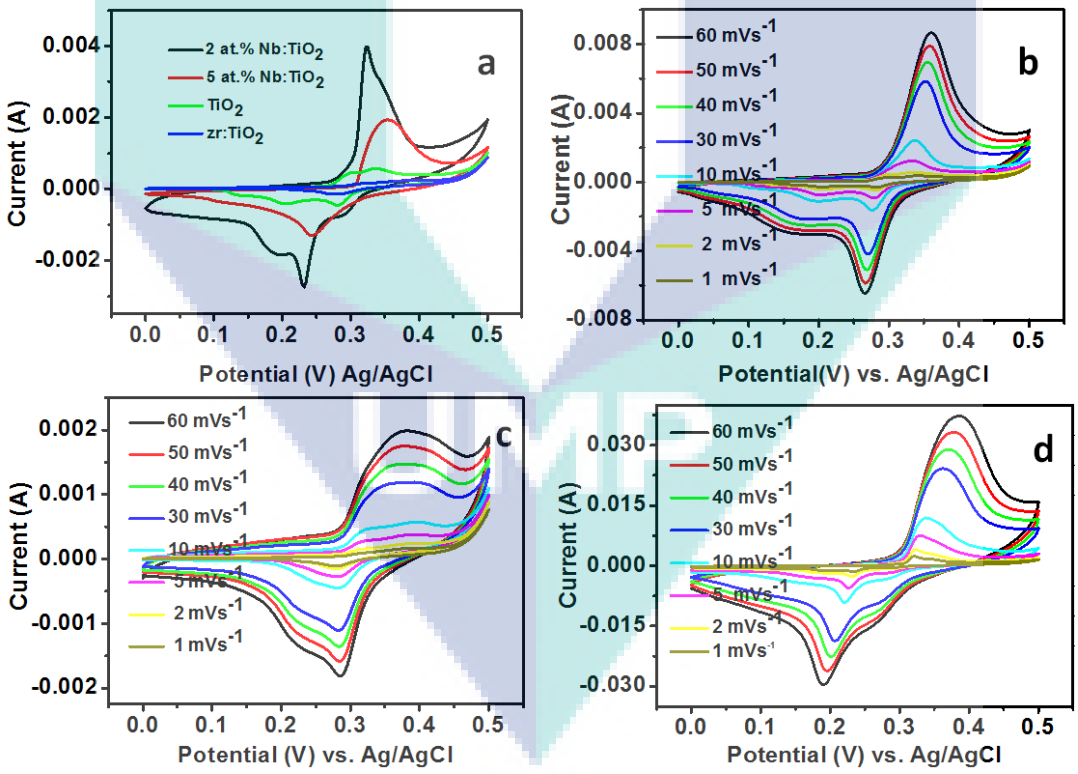

Figure 5:(a) shows the CV of the electrodes at a scan rate 2 mVs^{-1} (b, c & d) CV curves of pristine TiO_2, $Zr:TiO_2$ and $Nb:TiO_2$ electrodes in 3 M KOH aqueous electrolyte at scan rate between 1 to 60 mVs^{-1} with respect to Ag/AgCl reference electrode.

A high voltametric current (4 mA) is generated from 2at.%Nb:TiO_2 against <1 mA from pristine TiO_2 at 2 mVs^{-1} scan rate. It could be attributed to the enhanced faradic reaction due to the improved electrical conductivity of the Nb:TiO_2. However, the voltammetric current in the 5at.% Nb:TiO_2 dropped to ~50% (~2 mA) of that in 2at.% Nb:TiO_2 (4 mA), which most likely arise from the increased crystal defects in this sample and consequent charge trapping[29]. On the other hand, a much larger drop was observed in the voltametric current generated from Zr:TiO_2. The difference in anodic peak potential (E_A) and cathodic peak potential (E_C) is a measure of reversibility and internal resistance of the material[34]. The difference in potential ($E_C - E_A$) is found to be ~ 61 mV, 62 mV and 59 mV for pristine TiO_2, Zr:TiO_2, and Nb: TiO_2 respectively at 2 mVs^{-1}. The smaller value of ($E_C - E_A$) of Nb:TiO_2 indicates that the electrode material is highly reversible and has low internal resistance[35]. The ratio of area of the cathodic scan to that of anodic scan is a measure of coulombic efficiency and is found to be 93, 91, and 100% for pristine TiO_2, Zr:TiO_2 and 2at.% Nb:TiO_2, respectively. However, the coulombic efficiency reduced to 89% for 5at.% Nb:TiO_2.

Fig. 5(b-d) shows the CV curves of all electrodes at different scan rate from 2 – 60 mVs^{-1}. Because the 5at.% Nb:TiO_2 showed inferior performance than its 2at.% counterpart. The CV of the is in The CV profiles show oxidation (anodic) and reduction (cathodic) events at all scan rate, which are characteristics of pseudocapacitance. The anodic peak in the CV profile shifted towards positive potentials with increase in the scan rate and the cathodic peak to the negative potential on account of the polarization in the electrode material. The asymmetric and scan rate dependent shape of the CV profiles show that the origin of the capacitance is by fast and reversible faradic reaction. The C_S (Fg^{-1}) of the samples was estimated from the cathodic or anodic part of the CV data using the equation:

$$C_S = \frac{1}{mv(E_2 - E_1)} \int_{E_1}^{E_2} i(E)dE \qquad (2)$$

where E_1 and E_2 are the cutoff potentials in the CV curves and *i(E)* is the current at each potential, $E_2 - E_1$ is the potential window, *m* is the mass of the active material, and *v* is the scan rate. Fig. 7 show the variation of C_S with scan rate of all electrode materials. Slower scan rates enable higher diffusion of alkali cations into the nanowire electrodes thereby accessing a major fraction of the active site in the material and show high C_S. This makes 2 at.% Nb:TiO_2 active material for potential energy storage application.

In pseudocapacitive materials, scan rate (*v*) dependence of voltammetric current (*I*) is analyzed to determine whether the capacitance originates from surface redox reaction or from bulk diffusion. $I \propto v$ surface redox reaction and $I \propto \sqrt{v}$ for semi-infinite bulk diffusion. We observed a straight line for $i \propto \sqrt{v}$ (Fig. 6); therefore, bulk redox reaction occurred during the electrochemical reaction for both pristine TiO_2 and Nb:TiO_2, which is expected to be the source of the observed larger capacitance. But a straight line is observed for $I \propto v$ in case of Zr:TiO_2 (Fig. 6) which indicate that Faradic charge storage is limited only on the surface of the material. We observed a straight line for $i \propto \sqrt{v}$ (Fig. 6); therefore, bulk redox reaction occurred during the electrochemical reaction for both pristine TiO_2 and 2 at.% Ni:TiO_2, which is expected to be the source of the observed capacitance. The three fold raise in the capacitive behavior of 2 at.% Ni:TiO_2 could be due to the increased carrier charge density. In case of semi- infinite diffusion, *I* can be expressed by the Randle's –Sevcik equation at 25 °C,[36,37]

$$I = 2.69 \times 10^5 \times n^{3/2} \times D^{1/2} \times A \times C_0 \times \sqrt{v} \qquad (3)$$

where n is the number of electron transferred, A is the surface area of the electrode, D is the diffusion coefficient, v is the scan rate, and C_0 is the initial ion concentration. Based on slope of I vs $\sqrt{v}$ graph and Eq (3), diffusion coefficients of the electrolyte ions for the 2at.% Nb:TiO_2 and pristine TiO_2 electrode are found to be 1.08×10^{-13} and 9.16×10^{-15} cm^2s^{-1}, respectively; i.e., the Nb:TiO_2 offers two order of magnitude higher ion diffusivity than pristine TiO_2. The observed ion diffusivity for Nb:TiO_2 among the highest values reported for supercapacitor electrode materials[38,39].

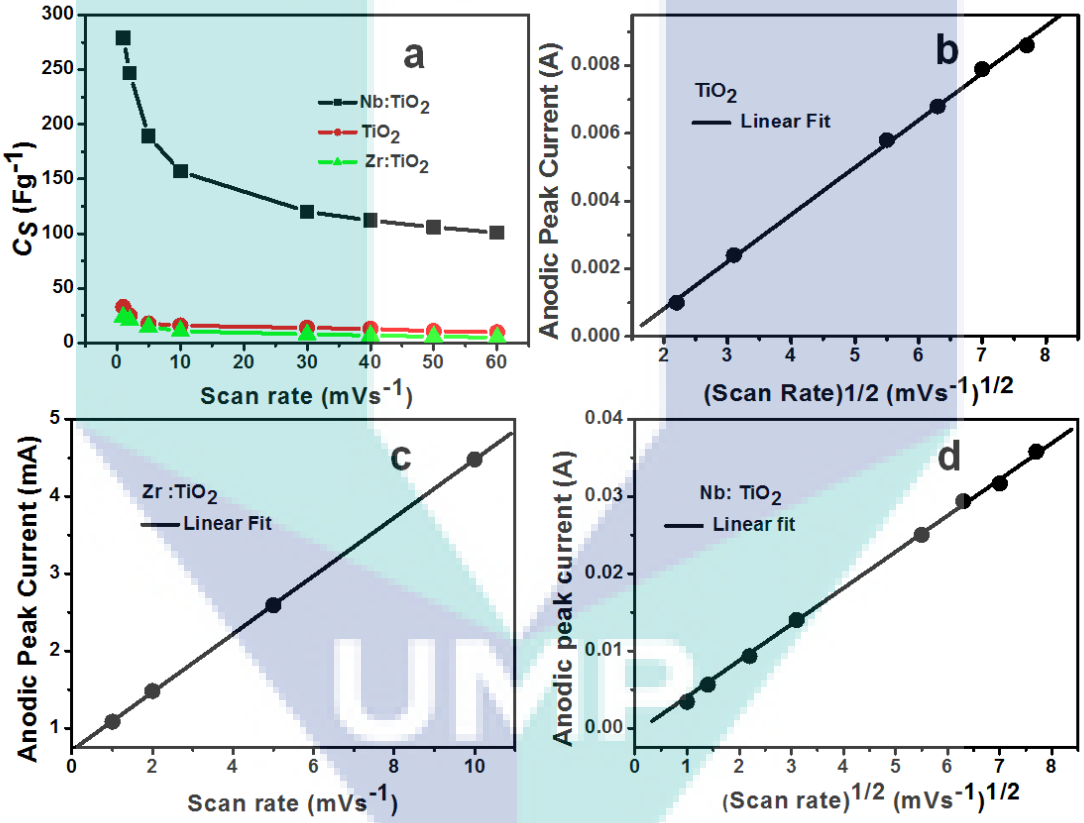

Figure 6: (a) Variation in C_S with scan rates;(b&d) anodic peak current verses square root of scan rate in pristine TiO_2 and Nb:TiO_2 indicating bulk diffusion of ions during the Faradic process; (c) anodic peak current verses scan rate in Zr:TiO_2

To isolate the supercapacitive performance of the active materials from the Ni foam substrate, the background capacitance of Ni foam was evaluated from the area under the CV curve. The area of the CV curve without using the active materials was ~ 1.3×10^{-4},

which is only ~0.01 % of the total area in the presence of it , thereby suggesting that contribution from the Ni foam is negligible in our experiment.

Fig.7 shows the CV curves of 2 at.% Ni:TiO_2 electrode as a function of scan rate.. The C_S calculated from CV curves at a scan rate 2 mVs^{-1} is 37, 184, and 91 F g^{-1} for pristine TiO_2, 2 at.% Ni:TiO_2 and 5 at.% Ni: TiO_2, respectively. Fig. 7c shows the variation of C_S with scan rate of both the electrode materials. High C_S was observed at slower scan rates because at such conditions higher diffusion of alkali cations into the nanowire electrodes are enabled thereby accessing a major fraction of the active site in the material.

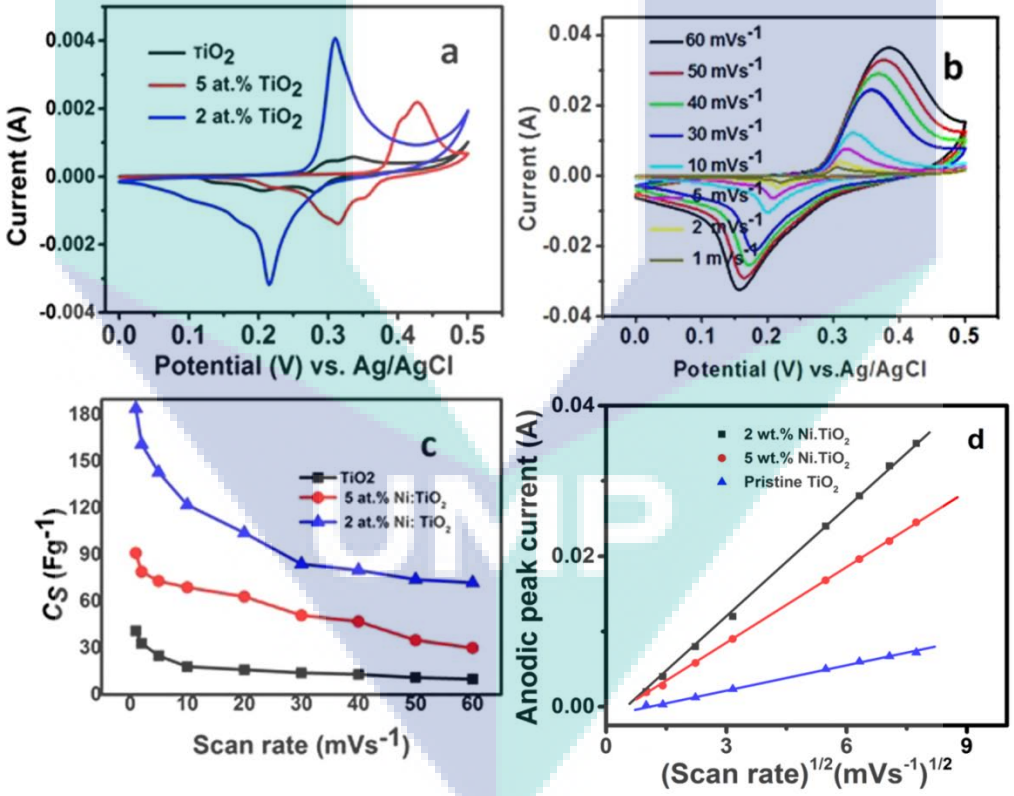

Figure 7: (a) shows the CV curves of the electrodes at 2mVs^{-1}; (b) CV curves of 2 at.% Ni:TiO_2 electrode in 3 M KOH aqueous electrolyte at a scan rate between 1 to 60 mVs^{-1} with respect to Ag/AgCl reference electrode;(b) Variation in C_S with scan rates;(d) anodic peak current verses square root of scan rate in pristine TiO_2 and 2 at.% Ni:TiO_2 indicating bulk diffusion of ions during the Faradic process.

4.3 Galvanostatic Charge- discharge study

Fig. 8 & 9 show the discharge curves for the pristine and doped nanowire electrodes in 3 M KOH aqueous electrolyte at a discharge current density 1 Ag^{-1} in the voltage range of 0–0.5 V. The longer discharge duration of the Nb:TiO_2 electrodes as compared to the other ones at the similar current density shows the enhanced pseudocapacitance of the Nb:TiO_2 electrodes. The potential drop during the discharge process, generally caused by the internal resistance (R) and incomplete faradic reaction of the device, was rather low (~14.8 mV) for Nb:TiO_2 nanowire electrodes. This lowering of R could be attributed not only due to the high electrical conductivity offered by donor impurity and also due to the one-dimensional nature of the electrode material (Fig. 2).

Fig. 8 shows the rate dependent discharge profile for the Nb:TiO_2 electrode in the potential window 0-0.5 V in 3 M KOH from which usually practically available C_S of a single electrode is calculated.The discharge curve is observed to be a combination of three processes, viz. (i) a fast initial potential drop followed by (ii) a slow potential decay, and (iii) a faster voltage drop corresponding to EDLC. The first two sections (Fig. 8b) are assigned to the reduction Ti^{4+} to Ti^{3+} as observed from the CVs. The clear non-linear shape of the discharge curves and the deviation from rectangular shape of the CV (Fig. 8d) reveal that the major contribution of C_S of Nb:TiO_2 electrode material originates from faradic reactions.

Fig. 9 shows the discharge curves of the pristine and Ni:TiO_2 electrodes in 3 M KOH aqueous electrolyte at a discharge current density 1 Ag^{-1} in the voltage range of 0–0.45 V. The discharge curve is a combination of three processes, viz. Fig. 9b shows the rate dependent discharge profile for the 2 at.% Ni:TiO_2 electrode in the potential window 0-0.45 V in 3 M KOH. Insets of Fig. 9b shows the C_S calculated from galvanostatic

discharge curves as a function of specific current density. The C_S decreased with increasing current density similar to that observed in the CV measurements.

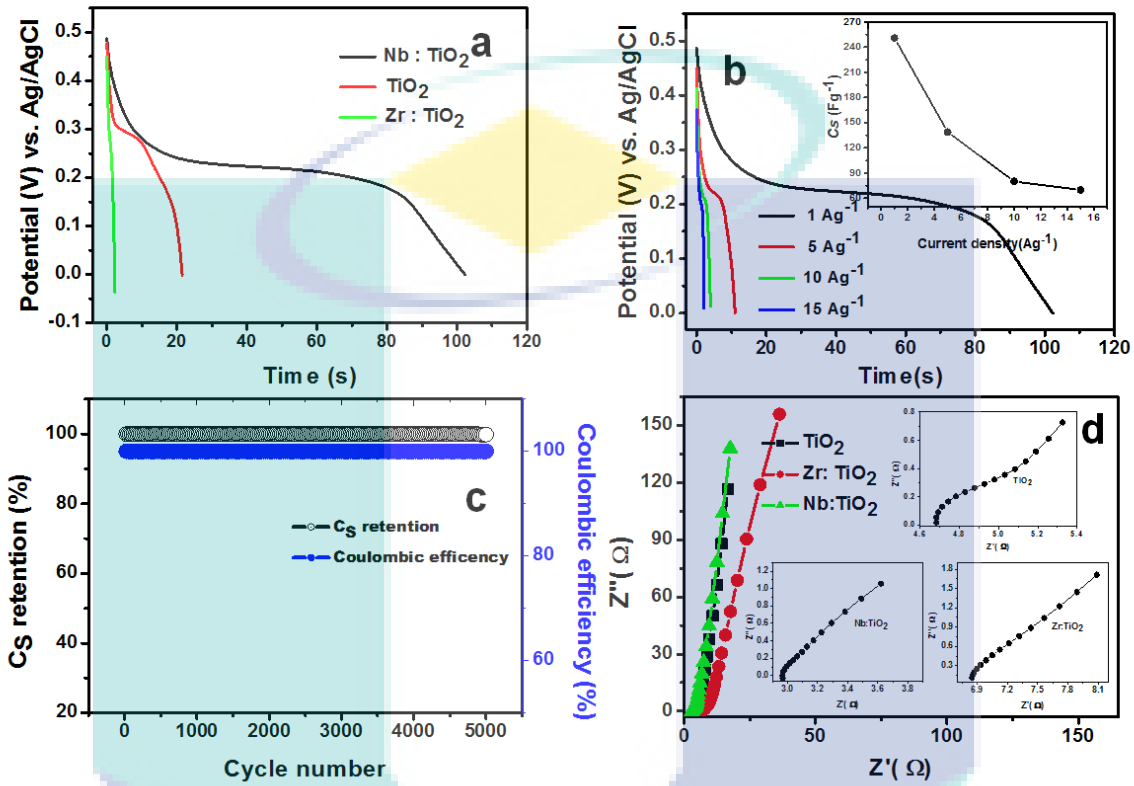

Figure 8: (a) discharge curves of all 3 electrodes in 3 M KOH aqueous electrolyte at a galvanostatic current density of 1 Ag^{-1} (b) discharge curves of Nb:TiO_2 electrode at different current densities in 3 M KOH aqueous electrolyte (c)Dependence of discharge C_S and Coulombic efficiency as a function of charge discharge cycle numbers (d) Nyquist plot for all 3 electrodes at open circuit potential; inset show the expanded high frequency region.

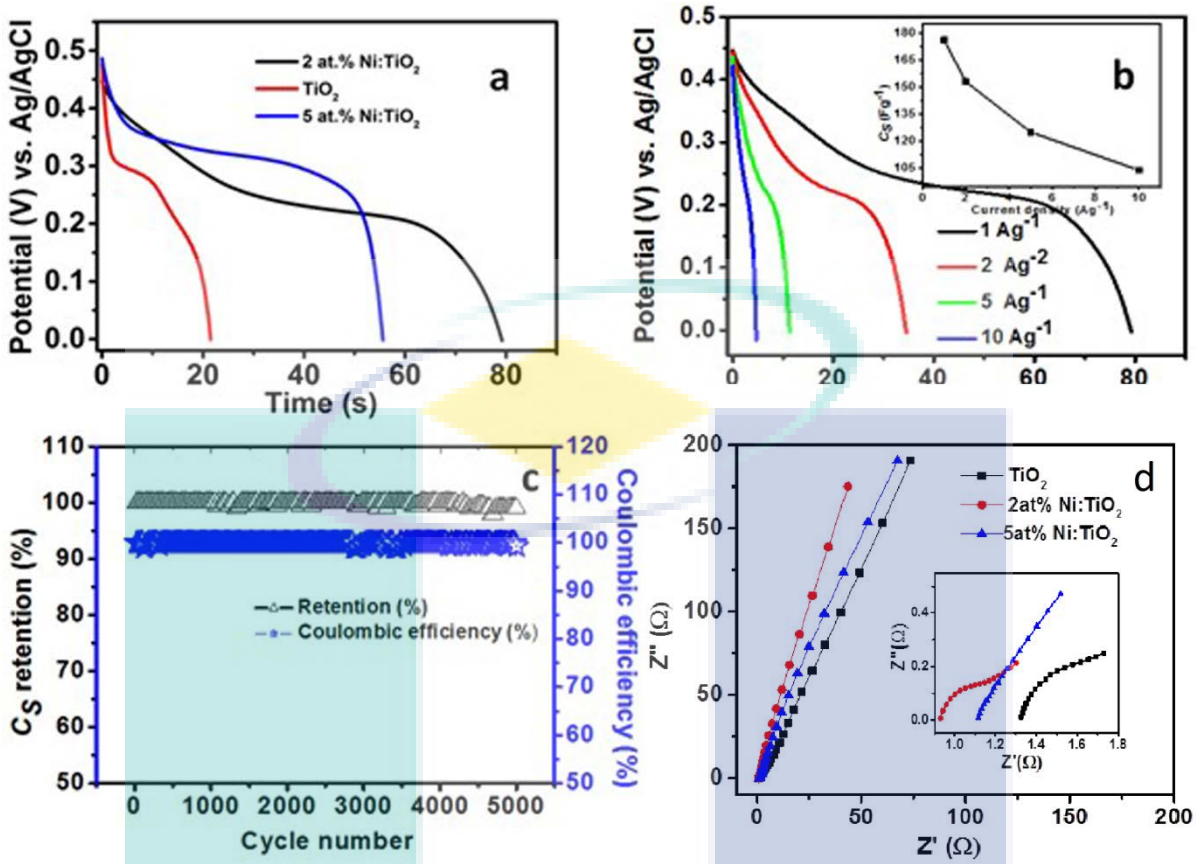

Figure 9: (a) discharge curves of electrodes in 3 M KOH aqueous electrolyte at a galvanostatic current density of 1 Ag^{-1} (b) discharge curves of 2 at.% $Ni:TiO_2$ electrode at different current densities in 3 M KOH aqueous electrolyte; inset shows the variation of C_S with current density; (c) Dependence of discharge C_S and Coulombic efficiency as a function of charge discharge cycle numbers (d) Nyquist plot for electrodes at open circuit potential; inset show the expanded high frequency region.

The C_S was calculated from the charge – discharge curves using the relation

$$C_S = \frac{It}{m\Delta V} \qquad (4)$$

where I, t, m and ΔV are applied current, time, active mass, and potential range of the charging and discharging events, respectively. Insets of Fig. 8b shows the C_S calculated from galvanostatic discharge curves as a function of specific current density. The C_S

decreased with increasing current density similar to that observed in the CV measurements. The contribution of C_S from the substrate was also studied in 3 M KOH from the discharge curves without using the nanowires. The discharge time was 5 s for Ni foam alone; thereby demonstrating that capacitive contribution from the substrate could be neglected.

Effects of the high crystallinity and clear insertion/exertion pathways of the electrospun Nb:TiO_2 nanowires are more evident in the cycling stability of the electrodes fabricated in this study. Fig. 8c and Fig.9c show the stability of electrochemical cycling of the Nb:TiO_2 nanowires and Ni:TiO_2 nanowires. The electrodes showed good cycling behaviour with ~100% retention in C_S at the end of 5000 cycles. The electrode was also physically stable; no peeling-off of the electrode material from current collector was observed even after 5000 cycles. The Coulombic efficiency calculated from ratio of the discharging to the charging times during the charge–discharge cycling was ~100% and remind practically same during cycling.

4.4 Electrochemical impedance spectroscopy

The EIS measurements were carried out to determine the electrode kinetics. Figure 8d and figure 9d show the Nyquist plots of nanowire electrodes determined by electrochemical impedance spectroscopy (EIS) in the frequency range 100 kHz – 0.01 Hz at open circuit potential in 3 M KOH. The EIS spectra of a SC electrode usually divided into three segments following three processes; (i) the bulk resistance of the device (R_S), synonymously called equivalent series resistance (ESR) at high frequency (> 1kHz); (ii) capacitive effects at intermediate frequencies (1 – 0.1 kHz); and (iii) Warburg diffusion resulting from the frequency dependence of ion diffusion/ transport in the electrolyte at the low frequencies (<0.1 Hz). The R_S is a combination of (i) electrolyte resistance, (ii)

intrinsic resistance of the electro active material, and (iii) the contact resistance between the active material and the current collector that determines the high frequency off-set of the EIS spectrum. The value of R_S determined from the high frequency off-set of the EIS spectra is ~ 2.8 Ω, 0.95 Ω, 4.5 Ω and 6.7 Ω for Nb:TiO_2, Ni:TiO_2, Zr:TiO_2 and pristine TiO_2 respectively. The lower R_S value of Nb:TiO_2 could be attributed to the high electrical conductivity of the present Nb:TiO_2 nanowires in addition to the one-dimensional morphology and ultrafine wire diameter.

Similarly the electrochemical performance of AC electrode was also evaluated in a three electrode configuration . The CV curves of the AC electrode at different scan rates in 3 M KOH aqueous electrolyte shows nearly rectangular shapes, suggesting that the AC electrode is an excellent choice to fabricate electric double layer capacitance (EDLC). The C_S of the material is estimated at 82 Fg^{-1}. Furthermore, the galvanostatic charge discharge curves of the AC measured at different current densities are symmetric and linear, which clearly shows the EDLC of the AC electrode. The C_S values of the AC electrodes are estimated using the equation 4 to be 82, 80, and 74 at 1 Ag^{-1}, 2 Ag^{-1} and 5 Ag^{-1} respectively.

4.5 Practical Asymmetric Supercapacitor

To evaluate the capacitive performance of the Nb:TiO_2 electrode in a full device configuration, an asymmetric supercapacitor (ASC) device was fabricated by using Nb:TiO_2 as the anode activated carbon (AC) as cathode. It is imperative to understand the properties of the pseudocapacitive and carbon electrodes separately for fabrication ASCs for optimum performance. This is because an ASC is equivalent to two capacitors in series whose reciprocal of the effective capacitance is equal to the sum of the reciprocals of the individual capacitances $\left(1/C_{eff} = 1/C_{anode} + 1/C_{cathode} \right)$. This relation follows that the effective

capacitance will be lower than the lowest individual capacitance. Therefore, both electrodes of ASCs should have similar capacitance for maximum effective capacitance[26]. The similarity in capacitance follows a charge balance (as charge $q = CV$) $q_+ = q_-$, where q_+ is the charge stored at the anode and q_- is that at the cathode. The charge on each electrode is given by $q = C_S \times \Delta V \times m$ [27], where ΔV is the potential window, from which the mass on the respective electrode for optimum performance follows [28,26]

$$\frac{m_-}{m_+} = \frac{C_{S+}(PC) \times \Delta V_+}{C_{S-}(EDLC) \times \Delta V_-}. \quad (5)$$

On the basis of the C_S values and potential windows of the Nb:TiO_2 and AC electrodes determined separately as explained above, the optimised mass ratio for fabrication of ASC was calculated to be ~1.5. A total of four ASCs were fabricated with cathode mass-loading up to 3.7 mg and anode mass-loading up to 2.5 mg to confirm the consistence of the results. A couple of symmetric EDLC using the AC electrodes (mass loading of ~4.2 mg on each electrodes) was fabricated as a control device. The devices had a geometric surface area of ~1cm^2.

Fig. 10 (a&b) shows the CV curves of the AC//AC symmetric EDLC and the Nb:TiO_2//AC ASCs devices as a function of scan rates, respectively. The ASC cell voltage can be expressed as the sum of the potential window of Nb:TiO_2 anode and AC cathode, which shows that potential window is between 0.5 V and -1.0 V vs. Ag/AgCl. Therefore, the Nb:TiO_2//AC device could achieve a maximum voltage of 1.5 V. Nearly rectangular shape and scan independent shape of CV curves (Fig. 10a) of the symmetric capacitors shows that the capacitance originates from EDLC. In addition, no scan rate dependence on C_S was observed (Inset of Fig. 6a). On the other hand, the CV curves of the ASC (Fig. 10 b) exhibited regions with and without redox peaks characterizing faradic pseudocapacitance and EDLC, respectively. The inset of Fig. 6b shows the C_S calculated

from the CV curves. A scan rate dependence on C_S was observed thereby revealing that the charge storage capabilities of the present ASC dominated by the Nb:TiO_2 electrode material.

The electrochemical performance was also measured by galvanostatic charge-discharge at current densities from 1 to 15 Ag^{-1}. Fig. 10(c&d) shows the first three charge-discharge cycles at a current density of ~1 Ag^{-1} of the EDLC and ASC devices. Maximum achievable potential window in the EDLC was ~1.2 V whereas that in the ASC was ~1.5 V. The additional voltage (0.3 V) achieved in the ASC is expected to originate from the pseudocapacitive reaction in the Nb:TiO_2 electrode. Figure 10 (e&f) are the discharge curves at different current densities to evaluate the rate capability of the devices and quantify the C_S. The insets of the respective figures show the variation of C_S as a function of current density determined following the Eq (4). The C_S decreases with increase in current density because the movements of electrolyte ions are limited to the surface of the electrode at high current densities whereas bulk diffusion occurs at lower values. The maximum C_S of symmetric EDLC was 17 Fg^{-1} at a discharge current density of 1 Ag^{-1} whereas that of ASC was nearly three times higher (52 Fg^{-1}). Therefore, due to the higher V and C_S, ASC is expected to have more than three-fold charge storage capability than the symmetric EDLC.

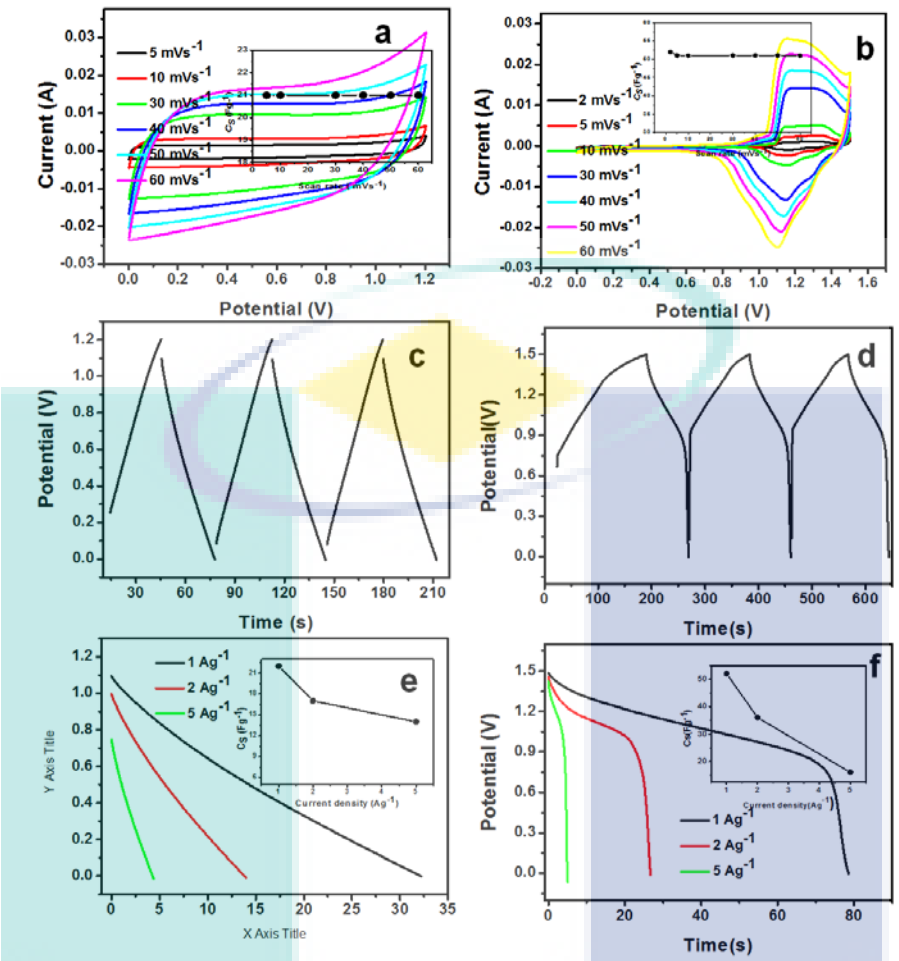

Figure 10: (a) The CV data of the AC//AC symmetric capacitor in 3 M KOH aqueous electrolyte at scan rates between 5 and 60 mVs^{-1};inset shows variation C_S with scan rate (b) The CV data of the Nb:TiO_2 //AC asymmetric supercapacitor in 3 M KOH aqueous electrolyte at scan rates between 2 and 60 mVs^{-1};inset shows variation in C_S with scan rate (c) The first three charge – discharge curves of the AC//AC symmetric supercapacitor in 3 M KOH aqueous electrolyte at a galvanostatic current density of 1 Ag^{-1} (d) The first three charge – discharge curves of the Nb:TiO_2//AC asymmetric capacitor in 3 M KOH aqueous solution at a galvanostatic current density of 1 Ag^{-1} (e) The discharge curves of the AC//AC symmetric capacitor at different current densities in 3 M KOH aqueous electrolyte; inset variation of specific capacitance of the device calculated from discharge curves (f) The discharge curves of the Nb:TiO_2//AC asymmetric capacitor at different current densities in 3 M KOH aqueous solution; inset shows the variation of C_S of the device calculated from discharge curves.

The operational stability of the device was evaluated by galvanostatic CDC at (i) single current rating (~5 Ag^{-1}) and (ii) progressively varying current densities (1 – 5 Ag^{-1}). The ASC exhibited capacitive retention of ~100% and Coulombic efficiency of ~100% at the end of the 3000 cycles (Fig. 11a) at 1 Ag^{-1}. Fig. 11b shows the rate capability of the device at current densities 1, 2, and 5Ag^{-1}. The device retained nearly constant C_S upon cycling at each current density. After continuous cycling for 1500 cycles at different current densities and when the current density is brought back to 1 Ag^{-1} for the last 500 cycles, the C_S remained without any lose (Fig. 11b). The C_S retention at a high current rating is superior to those reported for asymmetric supercapacitors using AC as a anode (Table 3).

Fig. 7c shows the Nyquist plot of the EDLC and ASC devices determined by EIS in the frequency range 10 kHz – 0.01Hz at open circuit potential in the 3 M KOH electrolyte[29]. The value of R_S determined from the high frequency off-set of the EIS spectra for the ASC is ~0.45 Ω which is desirable for a high power density; whereas R_S of EDLC is 0.88 Ω. The E_S and P_S of the devices were calculated using the relations

$$\left.\begin{aligned} E_S &= \frac{1}{2} C_S V^2; \\ P_S &= \frac{Es}{\Delta t} \end{aligned}\right\} \qquad (6)$$

Fig. 11d shows the Ragone plot which relates the P_S with the E_S. The ASC delivered E_S of 16.3, 11.4 and 5.6 $Whkg^{-1}$ at P_S of 770, 1310, and 1900 Wkg^{-1}, respectively. On the other hand, performance of the control EDLC is much inferior. The EDLC delivered E_S of 4.9, 4.5 and 4.2 $Whkg^{-1}$ at P_S 180, 317 and 690 Wkg^{-1}, respectively.

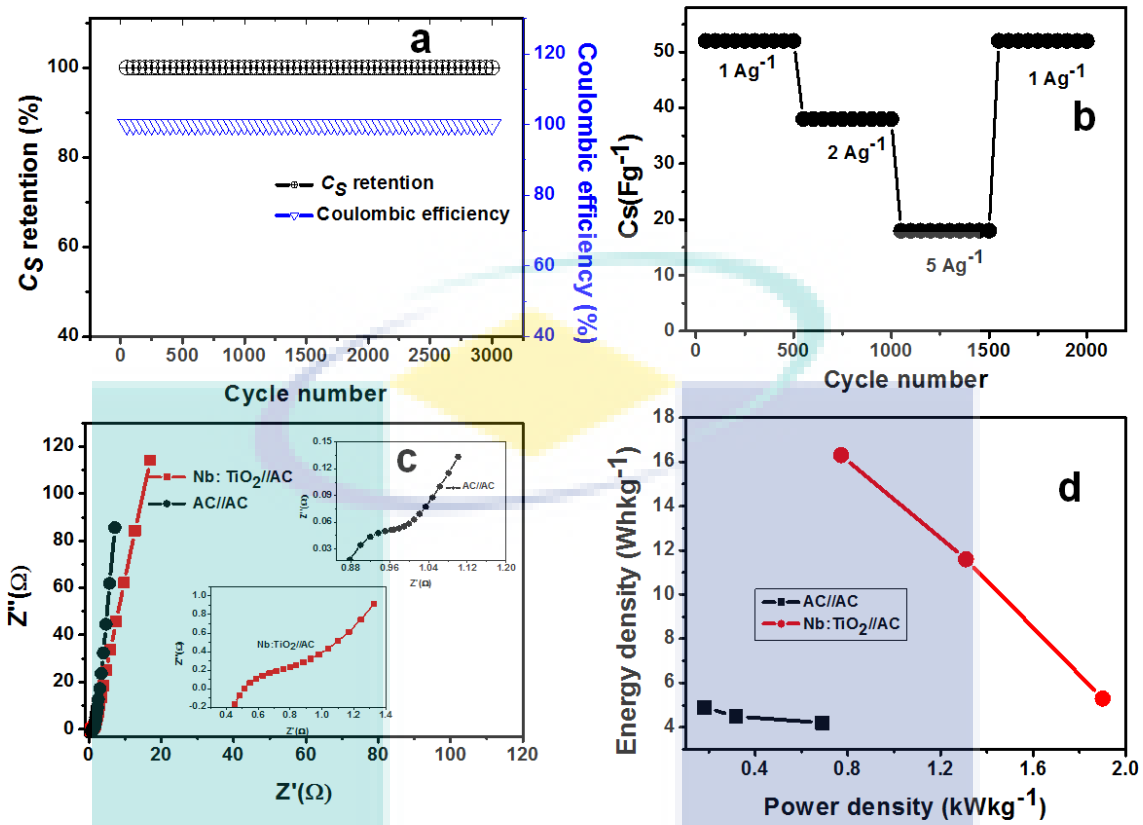

Figure 11: (a) Dependence of the discharge C_S and the columbic efficiency as a function of charge –discharge cycle numbers. The charge – discharge tests were performed at 5 Ag^{-1} in 3 M KOH aqueous electrolyte (b) dependence of the discharge C_S as a function of charge –discharge cycle numbers at progressively varying current densities.(c) Nyquist plot for both AC//AC and Nb:TiO_2//AC devices at open circuit potential. Insets show the expanded high frequency regions (d) Comparative Ragone plots of the symmetric and asymmetric supercapacitors.

Finally, we compare the performance of the present ASCs with other devices employing various TMOs as anode and the AC as the cathode in aqueous electrolyte (Table 3). Although there are many ASCs reported with TMO+ carbon nanotubes(CNT)/graphene as anode and CNT/graphene as cathodes, details of which are available in a recent review article, they are omitted from the present comparison for the sake of simplicity. Indeed, there are a number of devices such as $Ni(OH)_2$//AC[31] and

$Ni_{0.61}Co_{0.39}O$//AC ASCs[32] reported in literature with higher E_S; but all of them suffers from cycling stability than the performance achieved in this work.

Table 3: Comparison of energy storage parameters of ASC devices employing other TMOs reported in literature with that of the present Nb:TiO_2//AC ASCs. GR = graphene; NR = not reported; PMT = poly(3-methyl thiophene); PPy = polypyrrole.

ASC Configuration	Electrolyte	C_S (Fg^{-1})	Max V	E_S ($Wh.kg^{-1}$) @ P_S ($kW.kg^{-1}$)	C_S retention (%) /cycle number	Ref.
$Ni(OH)_2$//AC	6M KOH	105	1.6	36.2@0.1	92/1000	44
$Ni_{0.61}Co_{0.39}O$//AC	2M KOH	130.2	1.5	36.5@0.1	62.16/1000	45
Co_3O_4//AC	6M KOH	81	1.5	24.9@0.2	90/5000	68
Fe_3O_4//AC	6M KOH	37	1.2	NR	82/500	69
Ni_3S_2//AC	2M KOH	55.8	1.6	19.8@0.8	90/5000	70
$Ni_xCo_{3-x}O_4$//AC	2M KOH	105	1.6	37.4@0.2	82.8/3000	71
Ni-Co-Cu oxy hydroxide//AC	1M NaOH	58	1.8	NR	94.5/4000	72
Co_3O_4@NiOH //AC	6M KOH	110.6	1.7	41.9@0.4	81/1000	73
α–Bi_2O_3//AC	Li_2SO_4	29	1.6	10.2@0.8	72/1000	74
$NiMoO_4.xH_2O$//AC	2M KOH	96.7	1.6	34.4@0.1	80.6/1000	75
MnO_2-C//AC	0.5M $NaSO_4$	56.8	2	30.6@0.2	6/5000	76
$Ni(OH)_2$-TH-NH_3	NR	87.8	1.6	32.7@0.071	NR	77
MnO_2-AC//AC	1M Na_2SO_4	50.6	2	9.7@0.1	86/1000	78
PMT/MWNT//AC	$TEABF_4$	38.5	2.5	33.4@NR	85/1200	79
RuO_2/TiO_2//AC	1M KOH	46	1.4	12.5@0.1	90/1000	80
Co_3O_4-rGO//AC	6M KOH	114.1	1.5	35.7@0.2	95/1000	81
λ–MnO_2//AC	1M $LiSO_4$	53	2.2	36@0.3	NR	82
$Co(OH)_2$//AC	6M KOH	38.9	1.6	13.6@0.1	NR	83
Co_3O_4//AC	6M KOH	175	1.4	47.6@1.4	97/2000	84

$Ni(OH)_2$/GN/NF//AC	6M KOH	80	1.4	11.1@NR	NR	85
$LiMn_2O_4$//AC	1M $LiSO_4$	NR	1.8	29.8@0.09	91/1000	86
α–$Ni(OH)_2$//AC	2M KOH	127	1.2	42@0.1	82/1000	87
$NiCo_2O_4$//AC	1M NaOH	NR	1.7	17.7@NR	100/2000	88
$NiMoO_4$-$CoMoO_4$//AC	2M NaOH	80	1.4	28@0.1	92/1000	89
Co_3O_4//AC	6M KOH	107.3	1.5	34@0.22	98/1500	90
MnOOH@RGO//AC	6 M KOH	115.6	1.6	41.1@0.4	98/5000	91
Nb:TiO_2//AC	3M KOH	52	1.5	16.3@0.77	100/5000	This work

The higher E_S with high cycling stability could be attributed to the high electrical conductivity of the highly crystalline nanowires electrode. The Nb:TiO_2 based device shows 100% retention at the end of 5000 cycles which is suitable for a commercial device. Moreover, the current device could achieve a higher potential window of ~1.5 V in environmentally benign and low cost aqueous KOH electrolyte, which is comparable to those of commercial alkaline batteries. The potential window of the present Nb:TiO_2-based device could be increased further using proper another cathode material or using composite anode in the same electrolyte.

CHAPTER VII

SUMMARY AND RECOMMENDATIONS

In conclusion, we have shown that Nb:TiO_2 nanowires have an order of magnitude higher specific capacitance than pristine Ni:TiO_2, and Zr:TiO_2, which could be assigned to its improved electrical conductivity. Cyclic voltammetric measurements show that the superior electrical conductivity of Nb:TiO_2 help the electrode to achieve two orders of magnitude higher ion diffusivity (1.08×10^{-13} cm^2s^{-1}) than that offered by the other electrodes in this study (9.16×10^{-15} cm^2s^{-1}) and has 100% Coulombic efficiency. The improved electrical conductivity, ion diffusivity, and Coulombic efficiency enable the Nb:TiO_2 electrode to show constant capacitance for over 5000 cycles. A practical supercapacitor fabricated in asymmetric configuration using the Nb:TiO_2 as anode and activated carbon as cathode gave energy densities of 16.3, 11.4 and 5.6 $Whkg^{-1}$ at power densities of 770, 1310, and 1900 Wkg^{-1}, respectively, which are much superior to a control device fabricated using activated carbon as its both electrodes. High abundance of TiO_2 in the earth's crust and promising results achieved herewith offer unique opportunities to develop practical supercapacitors at lower costs.

The work described here only considered two dopants; tungsten doping could be better based on the electron donating ability. The usefulness of the tungsten doped TiO_2 to be tested.

Reference:

1. Chen, S., et al., Nanostructured morphology control for efficient supercapacitor electrodes. Journal of Materials Chemistry A, 2013. **1**(9): p. 2941-2954.

2. Lu, Q., J.G. Chen, and J.Q. Xiao, Nanostructured Electrodes for High-Performance Pseudocapacitors. Angewandte Chemie International Edition, 2013. **52**(7): p. 1882-1889.

3. Park, S., M. Vosguerichian, and Z. Bao, A review of fabrication and applications of carbon nanotube film-based flexible electronics. Nanoscale, 2013. **5**(5): p. 1727-1752.

4. Rauda, I.E., et al., Enhancing pseudocapacitive charge storage in polymer templated mesoporous materials. Accounts of chemical research, 2013. **46**(5): p. 1113-1124.

5. Shukla, A. and T.P. Kumar, Wiley Interdiscip. Rev. Energy Environ, 2013. **2**: p. 14-30.

6. Vidhyadharan, B., et al., Superior supercapacitive performance in electrospun copper oxide nanowire electrodes. Journal of Materials Chemistry A, 2014. **2**(18): p. 6578.

7. Jiang, J., et al., Recent advances in metal oxide-based electrode architecture design for electrochemical energy storage. Advanced Materials, 2012. **24**(38): p. 5166-5180.

8. Zhang, L.L. and X. Zhao, Carbon-based materials as supercapacitor electrodes. Chemical Society Reviews, 2009. **38**(9): p. 2520-2531.

9. Conway, B.E., Transition from "supercapacitor" to "battery" behavior in electrochemical energy storage. Journal of the Electrochemical Society, 1991. **138**(6): p. 1539-1548.

10. Tan, Y.B. and J.-M. Lee, Graphene for supercapacitor applications. Journal of Materials Chemistry A, 2013. **1**(47): p. 14814-14843.

11. Li, H., et al., Theoretical and experimental specific capacitance of polyaniline in sulfuric acid. Journal of Power Sources, 2009. **190**(2): p. 578-586.

12. Wei, W., et al., Manganese oxide-based materials as electrochemical supercapacitor electrodes. Chem Soc Rev, 2011. **40**(3): p. 1697-721.

13. Krishnan, S.G., et al., Characterization of MgCo2O4 as an electrode for high performance supercapacitors. Electrochimica Acta, 2015. **161**: p. 312-321.

14. D. Yu, Q. Qian, L. Wei, W. Jiang, K. Goh, J. Wei, J. Zhang, and Y. Chen, *Chem. Soc. Rev.*, 2015, **44**, 647–662.

15. D. R. Rolison and L. F. Nazar, *MRS Bull.*, 2011, **36**, 486–493.

16. D. A. J. Rand, *J. Solid State Electrochem.*, 2011, **15**, 1579–1622.

17. N.-S. Choi, Z. Chen, S. a Freunberger, X. Ji, Y.-K. Sun, K. Amine, G. Yushin, L. F. Nazar, J. Cho, and P. G. Bruce, *Angew. Chem. Int. Ed. Engl.*, 2012, **51**, 9994–10024.

18. S. Liu, S. Sun, and X.-Z. You, *Nanoscale*, 2014, **6**, 2037–45.

19. P. J. Hall, M. Mirzaeian, S. I. Fletcher, F. B. Sillars, A. J. R. Rennie, G. O. Shitta-bey, G. Wilson, and R. Carter, *Energy Environ. Sci.*, 2010, **3**, 1238–1251.

20. H. Li, J. Wang, Q. Chu, Z. Wang, F. Zhang, and S. Wang, *J. Power Sources*, 2009, **190**, 578–586.

21. J. Tian, Z. Zhao, A. Kumar, R. I. Boughton, and H. Liu, *Chem. Soc. Rev.*, 2014, **43**, 6920 – 6937.

22. R. Jose, V. Thavasi, and S. Ramakrishna, *J. Am. Ceram. Soc.*, 2009, **92**, 289–301.

23. M. V Reddy, G. V. S. Rao, and B. V. R. Chowdari, *Chem. Rev.*, 2013, **113**, 5364 – 5457.

24. Y. Furubayashi, T. Hitosugi, Y. Yamamoto, K. Inaba, G. Kinoda, Y. Hirose, T. Shimada, and T. Hasegawa, *Appl.Phys. Lett.*, 2005, **86**, 1–3.

25. F. Fabregat-santiago, E. M. Barea, J. Bisquert, G. K. Mor, K. Shankar, and C. a Grimes, *J. Am. Chem. Soc.*, 2008, **130**, 11312–11316.

26. P. S. Archana, A. Gupta, M. M. Yusoff, and R. Jose, *Phys. Chem. Chem. Phys.*, 2014, **16**, 7448–54.

27. P. S. Archana, A. Gupta, M. M. Yusoff, and R. Jose, *Appl. Phys. Lett.*, 2014, **105**, 153901–5.

28. P. S. Archana, E. Naveen Kumar, C. Vijila, S. Ramakrishna, M. M. Yusoff, and R. Jose, *Dalt. Trans.*, 2012, **42**, 1024–1032.

29. P. S. Archana, R. Jose, T. M. Jin, C. Vijila, M. M. Yusoff, and S. Ramakrishna, *J. Am. Ceram. Soc.*, 2010, **93**, 4096–4102.

30. T. Hitosugi, H. Kamisaka, K. Yamashita, H. Nogawa, Y. Furubayashi, S. Nakao, N. Yamada, A. Chikamatsu, H. Kumigashira, M. Oshima, Y. Hirose, T. Shimada, and T. Hasegawa, *Appl. Phys. Express*, 2008, **1**, 1112031–1112033.

31. S. Ramakrishna, R. Jose, P. S. Archana, a. S. Nair, R. Balamurugan, J. Venugopal, and W. E. Teo, *J. Mater. Sci.*, 2010, **45**, 6283–6312.

32. P. S. Archana, R. Jose, C. Vijila, and S. Ramakrishna, *J. Phys. Chem. C*, 2009, **113**, 21538–21542.

33. B. Vidhyadharan, N. Khayyriah, M. Zain, I. I. Misnon, R. A. Aziz, J. Ismail, M. M. Yusoff, and R. Jose, *J. Alloys Compd.*, 2014, **610**, 143–150.

34. P. Vishnu Kamath and M. F. Ahmed, *J. Appl. Electrochem.*, 1993, **23**, 225–230.

35. L. Bing, Y. Huatang, Z. Yunshi, Z. Zuoxiang, and S. Deying, *J. Power Sources*, 1999, **79**, 277–280.

36. E. Shangguan, Z. Chang, H. Tang, X.-Z. Yuan, and H. Wang, *J. Power Sources*, 2011, **196**, 7797–7805.

37. X. Cao, J. Wei, Y. Luo, Z. Zhou, and Y. Zhang, *Int. J. Hydrogen Energy*, 2000, **25**, 643–647.

38. B. Shruthi, V. Bheema Raju, and B. J. Madhu, *Spectrochim. Acta. A. Mol. Biomol. Spectrosc.*, 2015, **135**, 683–9.

39. P. Tang, Y. Zhao, C. Xu, and K. Ni, *J. Solid State Electrochem.*, 2013, **17**, 1701–1710.

40. D. Zhang, K. Ryu, X. Liu, E. Polikarpov, J. Ly, M. E. Tompson, and C. Zhou, *Nano Lett.*, 2006, **6**, 1880–6.

41. P. Chen, G. Shen, Y. Shi, H. Chen, and C. Zhou, *ACS Nano*, 2010, **4**, 4403–4411.

42. Y. Q. Zhang, L. Li, S. J. Shi, Q. Q. Xiong, X. Y. Zhao, X. L. Wang, C. D. Gu, and J. P. Tu, *J. Power Sources*, 2014, **256**, 200–205.

43. F. Wang, S. Xiao, Y. Hou, C. Hu, L. Liu, and Y. Wu, *RSC Adv.*, 2013, **3**, 13059–13084.

44. J. Huang, P. Xu, D. Cao, X. Zhou, S. Yang, Y. Li, and G. Wang, *J. Power Sources*, 2014, **246**, 371–376.

45. Y. Wang, X. Zhang, C. Guo, Y. Zhao, C. Xu, and H. Li, *J. Mater. Chem. A*, 2013, **1**, 13290–13300.

46. G. Wang, Z. Y. Liu, J. N. Wu, and Q. Lu, *Mater. Lett.*, 2012, **71**, 120–122.

47. M. Salari, S. H. Aboutalebi, A. T. Chidembo, K. Konstantinov, and H. K. Liu, *J. Alloys Compd.*, 2014, **586**, 197–201.

48. X. Lu, G. Wang, T. Zhai, M. Yu, J. Gan, Y. Tong, and Y. Li, *Nano Energy*, 2012, **12**, 1690–1696.

49. M. Salari, S. H. Aboutalebi, A. T. Chidembo, I. P. Nevirkovets, K. Konstantinov, and H. K. Liu, *Phys. Chem. Chem. Phys.*, 2012, **14**, 4770–4779.

50. A. Ramadoss and S. J. Kim, *Carbon N. Y.*, 2013, **63**, 434–445.

51. S. Dong, X. Chen, L. Gu, X. Zhou, H. Xu, H. Wang, Z. Liu, P. Han, J. Yao, L. Wang, G. Cui, and L. Chen, *ACS Appl. Mater. Interfaces*, 2011, **3**, 93–98.

52. G. D. Moon, J. B. Joo, M. Dahl, H. Jung, and Y. Yin, *Adv. Funct. Mater.*, 2014, **24**, 848–856.

53. C. C. Hu, C. W. Wang, T. H. Wu, and K. H. Chang, *Electrochim. Acta*, 2012, **85**, 90–98.

54. H. Li, Z. Chen, C. K. Tsang, Z. Li, X. Ran, C. Lee, B. Nie, L. Zheng, T. Hung, J. Lu, B. Pan, and Y. Y. Li, *J. Mater. Chem. A*, 2014, **2**, 229–236.

55. F. Fabregat-Santiago, H. Randriamahazaka, A. Zaban, J. Garcia-Cañadas, G. Garcia-Belmonte, and J. Bisquert, *Phys. Chem. Chem. Phys.*, 2006, **8**, 1827–1833.

56. H. Liang, F. Chen, R. Li, L. Wang, and Z. Deng, *Electrochim. Acta*, 2004, **49**, 3463–3467.

57. B. Chen, J. Hou, and K. Lu, *Langmuir*, 2013, **29**, 5911–5919.

58. W. W. Liu, X. B. Yan, and Q. J. Xue, *J. Mater. Chem. C*, 2013, **1**, 1413–1422.

59. D. Luo, Y. Li, J. Liu, H. Feng, D. Qian, S. Peng, J. Jiang, and Y. Liu, *J. Alloys Compd.*, 2013, **581**, 303–307.

60. P.-C. Chen, S.-J. Hsieh, J. Zou, and C.-C. Chen, *Mater. Lett.*, 2014, **133**, 175–178.

61. A. Ramadoss and S. J. Kim, *Int. J. Hydrogen Energy*, 2014, **39**, 12201–12212.

62. C. Huang, N. P. Young, and P. Grant, *J. Mater. Chem. A*, 2014, **2**, 11022–11028.

63. H. Zhou, Y. Zhong, Z. He, L. Zhang, J. Wang, J. Zhang, and C. N. Cao, *J. Alloys Compd.*, 2014, **597**, 1–7.

64. B. Zhang, R. Shi, Y. Zhang, and C. Pan, *Prog. Nat. Sci. Mater. Int.*, 2013, **23**, 164–169.

65. Y. Xiao, S. Liu, F. Li, A. Zhang, J. Zhao, S. Fang, and D. Jia, *Adv. Funct. Mater.*, 2012, **22**, 4052–4059.

66. Y. Gong, F. Gong, C. Wang, H. Zheng, and F. Li, *RSC Adv.*, 2015, **5**, 27266–27272.

67. Y. Xiao, A. Zhang, S. Liu, J. Zhao, S. Fang, D. Jia, and F. Li, *J. Power Sources*, 2012, **219**, 140–146.

68. C. Zhang, L. Xie, W. Song, J. Wang, G. Sun, and K. Li, *J. Electroanal. Chem.*, 2013, **706**, 1–6.

69. X. Du, C. Wang, M. Chen, Y. Jiao, and J. Wang, *J. Phys. Chem. C*, 2009, **113**, 2643–2646.

70. C.-S. Dai, P.-Y. Chien, J.-Y. Lin, S.-W. Chou, W.-K. Wu, P.-H. Li, K.-Y. Wu, and T.-W. Lin, *ACS Appl. Mater. Interfaces*, 2013, **5**, 12168–74.

71. X. Wang, C. Yan, A. Sumboja, and P. S. Lee, *Nano Energy*, 2014, **3**, 119–126.

72. C.-H. Lien, C.-C. Hu, C.-T. Hsu, and D. S.-H. Wong, *Electrochem. commun.*, 2013, **34**, 323–326.

73. C. Tang, X. Yin, and H. Gong, *ACS Appl. Mater. Interfaces*, 2013, **5**, 10574–82.

74. S. T. Senthilkumar, R. K. Selvan, M. Ulaganathan, and J. S. Melo, *Electrochim. Acta*, 2014, **115**, 518–524.

75. M.-C. Liu, L. Kang, L.-B. Kong, C. Lu, X.-J. Ma, X.-M. Li, and Y.-C. Luo, *RSC Adv.*, 2013, **3**, 6472–6478.

76. J.-G. Wang, Y. Yang, Z.-H. Huang, and F. Kang, *Carbon N. Y.*, 2013, **61**, 190–199.

77. Y. Tang, Y. Liu, S. Yu, Y. Zhao, S. Mu, and F. Gao, *Electrochim. Acta*, 2014, **123**, 158–166.

78. X. Zhang, X. Sun, H. Zhang, D. Zhang, and Y. Ma, *Mater. Chem. Phys.*, 2012, **137**, 290–296.

79. P. Sivaraman, A. R. Bhattacharrya, S. P. Mishra, A. P. Thakur, K. Shashidhara, and A. B. Samui, *Electrochim. Acta*, 2013, **94**, 182–191.

80. Y.-G. Wang, Z.-D. Wang, and Y.-Y. Xia, *Electrochim. Acta*, 2005, **50**, 5641–5646.

81. L.-J. Xie, J.-F. Wu, C.-M. Chen, C.-M. Zhang, L. Wan, J.-L. Wang, Q.-Q. Kong, C.-X. Lv, K.-X. Li, and G.-H. Sun, *J. Power Sources*, 2013, **242**, 148–156.

82. Y. Xue, Y. Chen, M.-L. Zhang, and Y.-D. Yan, *Mater. Lett.*, 2008, **62**, 3884–3886.

83. Y. Tang, Y. Liu, S. Yu, S. Mu, S. Xiao, Y. Zhao, and F. Gao, *J. Power Sources*, 2014, **256**, 160–169.

84. B. Vidyadharan, R. A. Aziz, I. I. Misnon, G. M. Anil Kumar, J. Ismail, M. M. Yusoff, and R. Jose, *J. Power Sources*, 2014, **270**, 526–535.

85. X. Wang, J. Liu, Y. Wang, C. Zhao, and W. Zheng, *Mater. Res. Bull.*, 2014, **52**, 89–95.

86. F. X. Wang, S. Y. Xiao, Y. S. Zhu, Z. Chang, C. L. Hu, Y. P. Wu, and R. Holze, *J. Power Sources*, 2014, **246**, 19–23.

87. J.-W. Lang, L.-B. Kong, M. Liu, Y.-C. Luo, and L. Kang, *J. Solid State Electrochem.*, 2009, **14**, 1533–1539.

88. C.-T. Hsu and C.-C. Hu, *J. Power Sources*, 2013, **242**, 662–671.

89. B. Senthilkumar, D. Meyrick, Y.-S. Lee, and R. K. Selvan, *RSC Adv.*, 2013, **3**, 16542–16548.

90. X. Zhang, Y. Zhao, and C. Xu, *Nanoscale*, 2014, **6**, 3638–46.

91. Y. Cao, Y. Xiao, Y. Gong, C. Wang, and F. Li, *Electrochim. Acta*, 2014, **127**, 200–207.

PATENT FILED: PI 2014701623 Dated: 17 June 2014 (The patent was filed based on the initial data secured prior to submission of this application)

Title: 1. High energy density supercapacitors from transition metal doped titanium dioxide nanostructures

FIELD OF INVENTION

The present invention relates toa method for fabricating supercapacitor electrode. More particularly, the present invention relates to a method for fabricating supercapacitor electrodebased on electrospuntitanium dioxide nanofibers.

BACKGROUND OF THE INVENTION

Supercapacitors represent a unique class of energy storage devices that can be categorized into three classes; electric double layer capacitors (EDLC), pseudocapacitors and hybrid capacitors. EDLCs store electrical energy via accumulation of electric charges at an electrical double layer formed at the interface between a polarisable electrode and an electrolyte. Carbon structures such as activated carbon, carbon nanotube and graphene are choice materials used in the development of EDLCs.No electron transfer takes place across the electrode interface during its operation; and therefore, this charge storage process is non-Faradic. Since charges are accumulated only at the electrical double layer formed, the capacitance of carbon based EDLC is lower than that of Faraday reaction based supercapacitors. Pseudocapacitors involve Faradic charge storage process facilitated by a redox reaction at the electrode-electrolyte interface. Hybrid capacitors, on the other hand, comprises of an electrode utilizing electrical double layer mechanism while another utilizes redox reaction.

The following properties are required in a pseudocapacitor in order to generate higher energy and power density; high specific surface area of the electrode to enable a large electrode-electrolyte interface for efficient redox reaction and high electrical conductivity to enable fast ion diffusivity and high rate charging and discharging. Transition metal oxides (TMOs) are especially advantageous as electrode material in pseudocapacitors as they show high faradaic pseudocapacitance and very low resistance, resulting in a high-output supercapacitor. Despite high capacitance of pseudocapacitors in comparison to EDLCs, EDLCs remain the most widely used capacitors. This is as pseudocapacitors present the following challenges; high manufacturing cost, difficulty of manufacturing process and high equivalent series resistance (ESR).

TMOs such as nickel oxide, copper oxide, manganese dioxide and ruthenium oxide are commonly used in the construction of supercapacitor electrodes as they excel in increasing electrical conductivity and chemical capacitance of the electrodes for use in energy storage devices. However, these TMOs present drawbacks including skin and respiratory irritant and in excess is toxic to the environment. Safe disassembling of used TMO containing devices for recycling purposes is difficult due to its irritancy. Irresponsibly discarded devices causes leaching of TMOs to the environment which is destructive to marine life and plants. Moreover, these TMOs are less-abundant in the earth's crust, which impart constraints in terms of supply and cost of raw materials. In order to solve the problem, an electrode composed of less toxic and environmentally friendly material is required.

Titanium is one of the top ten most abundant metal in the earth`s crust. Owing to its large abundance, comparatively low toxicity, environmental friendliness and desirable opto-electronic and catalytic properties, titanium dioxide is the candidate material for a number of applications including solar cells, batteries, photo-electrochemical cells, catalysis, paints and pigments and so on. However, titanium dioxide do not show any redox reaction in conventional alkaline electrolytes; and therefore, electrochemical application of titanium dioxide is limited to lithium ion batteries.

In order to improve electrochemical properties of titanium dioxide, modifications suggested in the past include coating of metal oxides onto titanium dioxide as disclosed in United States Patent No. 7670467. The prior art discloses a two steps method involving electrospinning process of titanium dioxide fibers and subsequent metal oxide coating of the electrospun fibers through immersing the titanium dioxide ultrafine fiber matrix substrate in a metal oxide precursor solution and applying a constant current potentiometry or a cyclic voltammetry to the solution. The electrochemical deposition methods utilized requires complex electrochemical set up for metal oxide coating on titanium dioxide fibers and further heat treatments of metal oxide coated fibers. Furthermore, the prior art have drawbacks in that the electrochemical performance of the electrode is influenced largely by both the fabrication step of titanium dioxide fibers and homogeneous deposition step of metal oxide particles throughout the fibers by the electrochemical deposition methods. Therefore, there is a need for a simpler process of transition metal deposition on titanium dioxide fiber that does not compromise the electrical performance of the electrode.

SUMMARY OF INVENTION

In accordance with the present invention, there is provided a method for fabricating supercapacitor electrode, the method is characterized by the steps of mixing of titanium alkoxide, polymer, transition metal salt solution and a suitable solvent (step **100**);adding an acid as a

hydrolysis catalyst into the mixture to obtain a stable suspension of hydrolysed solution (step **101**);stirring the resulting mixture to obtain a precursor solution for electrospinning (step **102**);electrospinning of precursor solution to obtain polymeric fibers (step **103**);collecting the polymeric fibers on a grounded rotating drum (step **104**);sintering the collected polymeric fibers in air at a temperature and sintering period to decompose polymers and obtain transition metal doped titanium dioxide nanofibers (step **105**);preparing a paste from a mixture of sintered transition metal doped titanium dioxide nanofibers, a suitable solvent and conductive carbon structure (step **106**);applying the paste onto a conducting substrate to form an electrode and drying the electrode at a temperature of 50 to 100 °C (step **107**); and fixing the paste onto the electrode (step **108**).

Preferably, the titanium alkoxide is selected from the group of titanium alkoxides comprising of titanium (IV) isopropoxide, titanium (IV) ethoxide and titanium (IV) butoxide or a mixtures thereof.

Preferably, the amount of titanium alkoxide ranges between 90 to 100 at %.

Preferably, the polymer is selected from the group comprising of polyvinylacetate, polyvinylpyrolidone, polyvinylideneflouride, polyaniline, poly(fluorophenyl)thiophene,poly(3-methyl)thiophene,poly(isothianaphthene), polyvinylalcohol, polyethyleneoxide and a mixture thereof, is dissolved in a solvent in which at least one solvent is selected from the group consisting of dimethyl formamide, acetone, tetrahydrofuran, ethanol, water and toluene or a mixture thereof.

Preferably, the transition metal salt solution is a salt solution of any transition metal in the periodic table which includes, but is not limited to niobium, tungsten, tantalum, nickeland zirconium.

Preferably, the amount of said transition metal ranges between 0 to 10 at %.

Preferably, the hydrolysis catalyst is selected from the group comprising of acetic acid, hydrochloric acid, hydrogen chloride gas, sulfuric acid, anhydride of sulfuric acid, nitric acid, anhydride of nitric acid, tartaric acid, propionic acid, phthalic anhydride, maleic acid, maleic anhydride, dodecylsuccinic anhydride, hexahydrophthalic anhydride, methyl endic anhydride, pyromellitic dianhydride, benzophenonetetracarboxylic anhydride, dichlorosuccinic anhydride, and chlorendic anhydride or a mixture thereof.

Preferably, the diameter of said titanium dioxide nanofibers is between 20 to 200 nm.

Preferably, the conductive carbon structure is selected from the group comprising of carbon black, graphene, activated carbon and carbon nanotubes.

Preferably, the paste comprises transition metal doped titanium dioxide nanofibers, a suitable solvent and conductive carbon structure combined in a mixing ratio ranging between 75:15:10 to 90:5:5.

Preferably, the solvent is selected from the group comprising of *n*-methylpyrolidone (NMP), decamethylcyclopentasiloxane (D5), parachlorobenzotrifluoride (PCBTF), *n*-propyl bromide (NPB), 1,2-trans dichloroethylene (DCE).

Preferably, the conducting substrate is selected from the group consisting of carbon paper, carbon sooth, nickel foam and stainless steel.

Preferably, the step of applying paste onto a conducting substrate is done by either; coating, brushing, spraying or dipping.

Preferably, the step of fixing the paste onto the conducting substrate is done by either; calendaring or pressing.

Preferably, the transition metal salt solution is substituted with metalloid salt solution of any metalloid in the periodic table which includes, but is not limited to antimony, tellurium and germanium.

BRIEF DESCRIPTION OF THE DRAWINGS

The accompanying drawings, which are incorporated in and constitute a part of the specification, illustrate embodiments of the invention and, together with the description, serve to explain the principles of the invention.

FIG. 1 is a flowchart of a method for the fabrication of semiconductor electrode based on electrospun titanium dioxide according to an embodiment of the present invention.

FIGS.2(a-b)are field emission scanning electron microscope and transmission electron microscope images of undoped titanium dioxide nanofibers fabricated based on the method of **FIG. 1**.

FIGS.3(a-b) are field emission scanning electron microscope and transmission electron microscope images of 2 at % niobium doped titanium dioxide nanofibers fabricated based on the method of **FIG. 1**.

FIGS.4(a-b) are field emission scanning electron microscope and transmission electron microscope images of 5 at % niobium doped titanium dioxide nanofibers fabricated based on the method of **FIG. 1**.

FIG.5is an X-ray fluorescence spectra of the 2 at % niobium doped titanium dioxideand 5 at %niobium doped titanium dioxide nanofibers prepared based on the method of **FIG. 1**.

FIGS.6arecyclic voltammograms of undoped titanium dioxide, 2 at % niobium doped titanium dioxide, 2 at % nickel doped titanium dioxide and 2 at % zirconium doped titanium dioxide nanofibers prepared based on the method of **FIG. 1**.

FIGS.7(a-d)are a collection of test results from electrochemical characterizations of 2 at % niobium doped titanium dioxide electrodes prepared based on the method of **FIG. 1**.
FIGS.8(a-f) are detailed electrochemical characterizations of activated carbon//activated carbon symmetric capacitor and 2 at % niobium doped titanium dioxide//activated carbon asymmetric supercapacitor prepared based on the method of **FIG. 1**.

DESCRIPTION OF THE PREFFERED EMBODIMENT

A preferred embodiment of the present invention will be described herein below with reference to the accompanying drawings. In the following description, well known functions or constructions are not described in detail since they would obscure the description with unnecessary detail.

It is an objective of this invention to provide a method to enhance the electrochemical properties of titanium dioxide (TiO_2). The method is on doping of transition metal ions in the titanium (Ti) host lattice to simultaneously control their conduction and valence band edges, which in return, controls the electrochemical properties of transition metal doped $TiO_2$and enhances its electron density for high or metallic conductivity. The present invention envisages a transition metal doped TiO_2 nanofibers as a part of the material for fabricating pseudo-capacitive electrode in supercapacitor devices. Reference is made to **FIG. 1**which shows a flowchart showing the steps involved in the preparation of transition metal doped TiO_2nanofibers.

Initially, a polymer is dissolved in a suitable solvent together with a titanium alkoxide and a transition metal salt solution as in step **100**. The polymer includes but is not limited to polyvinylacetate, polyvinylpyrolidone, polyvinylideneflouride, polyaniline, poly(fluorophenyl)thiophene,poly(3-methyl)thiophene,poly(isothianaphthene), polyvinylalcohol and polyethyleneoxide. The polymer is dissolved in a solvent which includes but is not limited to dimethyl formamide, acetone, tetrahydrofuran, ethanol, water and toluene. The titanium alkoxide includes but is not limited to titanium (IV) isopropoxide, titanium (IV) ethoxide and titanium (IV) butoxide. Preferably, the amount of said titanium alkoxide ranges between 90 to 100 at %. Titanium dioxide nanofiber is doped with any transition metals or metalloid in the periodic tablewhich includes, but is not limited to niobium, tungsten, tantalum,nickel andzirconium. Preferably, the amount of said transition metals ranges between 0 to 10 at %.

Next, an acidic hydrolysis catalyst is added into the mixtureuntil a stable suspension of a hydrolysed solution is obtained as in step **101**. The hydrolysis catalyst includes but is not limited to acetic acid, hydrochloric acid, hydrogen chloride gas, sulfuric acid, anhydride of sulfuric acid, nitric acid, anhydride of nitric acid, tartaric acid, propionic acid, phthalic anhydride, maleic acid, maleic anhydride, dodecylsuccinic anhydride, hexahydrophthalic anhydride, methyl endic anhydride, pyromellitic dianhydride, benzophenonetetracarboxylic anhydride, dichlorosuccinic anhydride and chlorendic anhydride.The mixture is stirred to obtain a precursor solution for electrospinning as in step **102**.

Thereon, the preparedprecursor solution is electrospun and collected on a grounded rotating drum as in step **103** and step **104**.

Thereon, the polymeric fibers generated are sintered in air at a temperature and sintering period to allow full decomposition of the polymers and growth of titanium dioxide as in step **105**. The sintering temperature and period is dependent on the polymer used.

The obtained transition metal doped TiO_2 nanofibers is mixed into a paste of transition metal doped titanium dioxide nanofibers, a suitable solvent and conductive carbon structure as in step **106**. The solvent includes but is not limited to *n*-methylpyrolidone (NMP), decamethylcyclopentasiloxane (D5), parachlorobenzotrifluoride (PCBTF), *n*-propyl bromide (NPB), 1,2-trans dichloroethylene (DCE).The conductive carbon structure includes but is not limited to carbon black, graphene, activated carbon and carbon nanotubes. Preferably, the mixing ratio ranges between range 75:15:10 to 90:5:5.

Thereon, the paste is applied onto a conductive carbon structure to form an electrode and dried as in step **107**. The conducting substrates include, but is not limited to carbon paper, carbon

sooth, nickel foam and stainless steel. The paste is applied using means that include, but is not limited to coating, brushing, spraying or dipping.

Finally, the paste is fixed onto the conducting substrate as in step **108**. The paste is fixed using means that include, but is not limited to calendaring and pressing.

The following examples illustrate the invention. The examples used herein are intended merely to facilitate an understanding of ways in which the embodiments herein may be practiced and to further enable those of skill in the art to practice the embodiments herein. Accordingly, the examples should not be constructed as limiting the scope of the embodiment herein.

Examples of the Experiments are illustrated as follows:

Procedures

In accordance with the present invention, for synthesis of niobium (Nb)-doped TiO_2 nanofibers, the precursor solution for electrospinning comprises polyvinyl acetate (PVAc), dimethyl formamide (DMF), titanium (IV) isopropoxide, niobium ethoxide and acetic acid.

4.5 g of PVAc (Mw 500,000) is dissolved in 11.5 wt % DMF together with titanium (IV) isopropoxide and niobium ethoxide. The Ti and Nb precursor amounts are calculated based on the number of atoms required for replacing a given number of Ti atoms by Nb atoms. The sol is prepared by the dropwise addition of 0.5 g of acetic acid. The resulting solution is stirred well and electrospun using an electrospinning machine at 25 kV accelerating voltage and 1 ml/hr flow rate. The polymeric fibers containing Ti^{4+} and Nb^{5+}ions, as a typical example, are collected on a grounded rotating drum placed approximately 10 cm below the spinneret. All the samples are sintered in air at 500 °C for 24 h to remove PVAc and allow nucleation and growth of TiO_2 particles in the fiber structure. Nickel (Ni)-doped and zirconium (Zr)-doped TiO_2nanofibers are developed using metal salts nickel chloride and zirconium oxychloride, respectively, by replacing niobium ethoxide in the method described above.

The working electrodes are prepared by mixing transition metal doped TiO_2nanofiberswith *n*-methylpyrolidone (NMP) andcarbon black (Super P®)in the ratio of 75:15:10 to form a paste. The resulting paste are coated on a nickel foam substrate, to form an electrode. The electrode is dried in an oven overnight at 70°C. The dried electrode is pressed at 5 tonne.

Results and Discussion

FIG.2, FIG. 3 and **FIG. 4**show the morphologies of doped and undoped TiO_2fibers examined using field emission scanning electron microscope (FESEM) and transmission electron microscope (TEM). The fibers were uniform with an average diameter of 150 nm. The continuous fibers having a smooth surface consist of grains of uniform sizes. Undoped TiO_2 fibers were featured by grains of larger diameter (approximately 50 nm). The doped fibers, on the other hand, were constituted by grains of lower diameter (approximately 10-30 nm) implying that the doping reduced the grain growth under similar processing conditions.

Particulate properties of the materials were studied using **Brunauer-Emmett-Teller** (BET) surface area measurements. Despite having similar fiber diameter, the BET surface area decreased with an increase in the Nb concentration. The BET surface area of the pureTiO_2, 2 at % Nb doped titanium dioxide(Nb:TiO_2) and 5 at % Nb:TiO_2samples were 45, 33 and 24 m^2/g, respectively. Consequently the pore size increased from 3 nm to 4 nm upon 5 at % doping. Reason for the lowering of surface area for fibers processed at similar conditions is assigned to the presence of niobium ions, which are heavier than titanium ions.

Presence of Nb in the samples was confirmed by X-ray fluorescence (XRF) measurements. **FIG. 5** shows the XRF patterns of samples containing Nb. The K_α and K_β lines of Ti were displayed in the XRF spectra at 4.5006 and 4.9236 keV, respectively. The K_α and K_β lines of Nb were observed in the spectra at 16.6086 and 18.1648 keV, respectively, and shown in the inset of **FIG. 5**. The intensities of the X-ray lines, both K_α and K_β, peak of Ti decreased and those of the Nb increased with doping concentration. Those observations indicate the Nb is dissolved in the titanium sub-lattice as expected.

FIG. 6shows the cyclic voltammograms (CV)of pure TiO_2, 2 at % Nb:TiO_2, 2 at % Ni:TiO_2 and 2 at % Zr:TiO_2 recorded in 3M KHO, from which their electrochemical cyclability could be evaluated. No electrochemical activity was observed for the pure $TiO_2$and 2 at % Zr:TiO_2; however, dramatic change is observed for the Nb and Ni-doped TiO_2 samples. The Nb and Ni-doped TiO_2samples shows oxidation (anodic) and reduction (cathodic) events indicative of the pseudocapacitive charge storage mechanism. The ratio between the charge stored during the oxidation and the reduction events, which is obtained from the respective integrated area under the CV curve, is a measure of Coulombic efficiency (η) of the system. The η of the 2 at % Nb:TiO_2 is calculated to be 98 % in 3M KOH electrolytes.

FIG. 7shows theCV curve **(a)**, charge discharge cycling **(b)**, specific capacitance with various scan rate**(c)** and stability of electrochemical cycling **(d)**of 2 at % Nb:TiO_2 nanofibers.

FIG. 7(a) represent the variation of CV curves as a function of potential scan rate. The CV curves marked lower slopes for lower scan rates, which indicate that lower scan rates allow longer duration for the anions to access the bulk of the electrode; thereby showing ideal capacitive behaviour. However, with the increase of scan rate the anodic peak shifts towards positive potentials and the cathodic peak shifts towards the negative potential as was observed conventionally. The specific capacitancenormally decreases with increasing scan rates due to the above reasons. The specific capacitance(C_s) of the samples were estimated from the cathodic or anodic part of the CV data using the equation:

$$C_s = \frac{1}{mv(E_2 - E_1)} \int_{E_1}^{E_2} i(E)dE$$

whereC_s is the specific capacitance,E_1 and E_2 are the cutoff potentials in the CV curves and $i(E)$ is the current of each potential, $E_2 - E_1$ is the potential window, m is the mass of the active material and v is the scan rate. **FIG. 7(c)** is the specific capacitanceof 2 at % Nb:TiO_2nanofibers at the scan rates in the 2 – 70 mV/s range of voltage window 0 – 0.6 V for the two electrolytes. The 3M KOH showed a specific capacitanceof approximately 200 Fg^{-1} at 2 mVs^{-1} scan rate. The specific capacitanceremained practically the same for higher scan rates (more than 30 mVs^{-1}) primarily because the ions movement is limited only to the surfaces of the electrode material at such conditions. The EDLC is the dominant mechanism at higher scan rates. Majority of active surfaces are utilized by the ions for charge storage at the lower scan rates (less than 5 mV/s), thereby resulting in higher specific capacitance. The reported specific capacitance here is the highest ever recorded in any TiO_2 materials.

The stability of the devices for long term operation was evaluated by calculating the variation in specific capacitance and Coulombic efficiency from galvanostatic charge-discharge cyclic under single and arbitrarily varying current densities for 5000 cycles. **FIG. 7(d)** shows typical variation of capacity retention as a function of cycle number. Under constant cycling of 5 Ag^{-1}, the asymmetric supercapacitorretained 96 % of specific capacitance over 5000 cycles, which make the device suitable for practical applications.

An asymmetric supercapacitor was assembled using 2 at % Nb:TiO_2 as anode and activated carbon(AC) as cathode in 3M KOH aqueous electrolyte2 at % Nb:TiO_2//AC asymmetric supercapacitors. A symmetric supercapacitor using AC (AC//AC symmetric supercapacitor)was also fabricated for comparison. One of the primary criteria for optimum performance from an asymmetric supercapacitor is the balance between mass loading of the two electrodes such that the charge involved in them are equal. An optimized mass loading ratio of 2.4 was calculated from the

specific capacitance and potential window of the 2 at % Nb:TiO_2 and the AC in single electrode configuration. The mass loading of AC was 3.2 mg/cm^2.

The CV curves of the AC//ACsymmetric and 2 at % Nb:TiO_2//ACasymmetric supercapacitors in 3M KOH aqueous solution at scan rates between 2 and 60 mVs^- at a potential of 1.4 Vis shown in**FIG. 8(a)** and **FIG. 8(b)**, respectively. Insets of **FIG. 8(a)** and **FIG. 8(b)**show the specific capacitance with various scan rate. The first three charge-discharge curves of AC//AC symmetric supercapacitor and 2 at % Nb:TiO_2//AC asymmetric supercapacitor in 3M KOH aqueous solution at a galvanostatic current density of Ag^{-1} is shown in**FIG. 8(c)** and **FIG. 8(d)**, respectively. Thedischarge curves AC//AC symmetric and 2 at % Nb:TiO_2//AC asymmetric supercapacitor at different current capacities in 3M KOH aqueous solution is shown in **FIG. 8(e)** and **FIG. 8(f)**,respectively. Insets of **FIG. 8(e)** and **FIG. 8(f)**illustrate the variation of specific capacitance of the device calculated from discharge curves.

The CV curves of the symmetrical device showed characteristic near rectangular shapes whereas that of the asymmetric supercapacitor exhibited a region of broad redox peaks characteristic of faradic pseudocapacitance and a region without any redox peaks characteristic of electric double layer capacitors (EDLC). The electrodes were stable and no oxygen evolution was observed from the surface of the electrode in the respective voltage windows. Variation of specific capacitance with scan rate was calculated from the CV curves and displayed in the insets of the respective graphs. The specific capacitance of the symmetrical device showed no variation with scan rate whereas that of the asymmetric supercapacitor showed a strong dependence on scan rate thereby indicating that overall performance of the asymmetric supercapacitor is dominated by the positive electrode.

The energy density (E) and power density (P) was calculated using the equation;

$$E = \frac{1}{2} C_s V^2; P = \frac{V^2}{4R_3 m}$$

where V is the charge-discharge potential window and m is the total mass of the electrode. The maximum energy density of the asymmetric supercapacitor was approximately 40 $Whkg^{-1}$ at a power density of approximately 3000 Wkg^{-1}, which is three folds higher than those of symmetrical supercapacitor (energy density of approximately 17 $Whkg^{-1}$ and a power density of approximately 690 Wkg^{-1}).

Therefore, this invention relates to conversion of TiO_2 electrochemically active by transition metal doping and fabrication of supercapacitor devices using the transition metal doped TiO_2 as a pseudocapacitive electrode. Pure TiO_2 is not electrochemically active. An asymmetric

supercapacitor with specific energy density three times that of symmetric capacitors based on conventional activated carbon has been developed as a typical example.

While embodiments of the invention have been illustrated and described, it is not intended that these embodiments illustrate and describe all possible forms of the invention. Rather, the words used in the specifications are words of description rather than limitation and various changes may be made without departing from the scope of the invention.

CLAIMS

1. A method for fabricating supercapacitorelectrode,is characterized by the steps of:
   a) mixing of titanium alkoxide, polymer, transition metal salt solution and a suitable solvent (step **100**);
   b) adding an acid as ahydrolysis catalyst into the mixtureto obtain a stable suspension of hydrolysed solution(step **101**);
   c) stirring the resulting mixture to obtain a precursor solution for electrospinning(step **102**);
   d) electrospinning of precursor solutionto obtain polymeric fibers (step **103**);
   e) collecting the polymeric fibers on a grounded rotating drum(step **104**);
   f) sintering the collected polymeric fibersin airat a temperature and sintering period to decompose polymers and obtain transition metal doped titanium dioxide nanofibers (step **105**);
   g) preparing a paste from a mixture of sintered transition metal doped titanium dioxide nanofibers, a suitable solventand conductive carbonstructure (step **106**);
   h) applying the paste onto a conducting substrate to form an electrode and drying the electrodeat a temperature of 50 to 100 °C (step **107**); and
   i) fixing the paste onto the electrode(step **108**).

2. The method as claimed in claim **1**, wherein said titanium alkoxideis selected from the group of titanium alkoxides comprising of titanium (IV) isopropoxide, titanium (IV) ethoxide andtitanium (IV) butoxide or a mixtures thereof.

3. The method as claimed in claim **2**, wherein the amount of said titanium alkoxide ranges between90 to 100 at %.

4. The method as claimed in claim **1**, whereinsaid polymeris selected from the group comprising of polyvinylacetate, polyvinylpyrolidone, polyvinylideneflouride, polyaniline, poly(fluorophenyl)thiophene,poly(3-methyl)thiophene,poly(isothianaphthene), polyvinylalcohol, polyethyleneoxideand a mixture thereof,is dissolved in a solvent in which at least one solvent is selected from the group consisting of dimethyl formamide, acetone, tetrahydrofuran, ethanol, water and toluene ora mixture thereof.

5. Themethod as claimed in claim **1**, whereinsaid transition metal salt solution is a salt solution of any transition metalin the periodic table which includes, but is not limited to niobium, tungsten, tantalum,nickelandzirconium.

6. The method as claimed in claim **1**, wherein the amount of said transition metal ranges between 0 to 10 at %.

7. The method as claimed in claim **1**, wherein said hydrolysis catalyst is selected from the group comprising of acetic acid, hydrochloric acid, hydrogen chloride gas, sulfuric acid, anhydride of sulfuric acid, nitric acid, anhydride of nitric acid, tartaric acid, propionic acid, phthalic anhydride, maleic acid, maleic anhydride, dodecylsuccinic anhydride, hexahydrophthalic anhydride, methyl endic anhydride, pyromellitic dianhydride, benzophenonetetracarboxylic anhydride, dichlorosuccinic anhydride, and chlorendic anhydrideor a mixture thereof.

8. Themethod as claimed in claim **1**, whereinthe diameter of saidtitanium dioxide nanofibers is between 20 to 200 nm.

9. The method as claimed in claim **1**, wherein said conductive carbon structure is selected from the group comprising of carbon black, graphene, activated carbon and carbon nanotubes.

10. The method as claimed in claim **1**, wherein the paste comprisestransition metal doped titanium dioxide nanofibers, a suitable solventand conductive carbon structure combined in a mixing ratio ranging between 75:15:10 to 90:5:5.

11. The method as claimed in claim **1**, wherein said solvent is selected from the group comprising of*n*-methylpyrolidone (NMP),decamethylcyclopentasiloxane (D5),

parachlorobenzotrifluoride (PCBTF), *n*-propyl bromide (NPB), 1,2-trans dichloroethylene (DCE).

12. The method as claimed in claim **1**, wherein said conducting substrate is selected from the group consisting of carbon paper, carbon sooth, nickel foam and stainless steel.

13. The method as claimed in claim **1**, wherein the step of applying paste onto a conducting substrateis done by either;coating, brushing, spraying or dipping.

14. The method as claimed in claim **1**, wherein the step of fixing the paste onto the conducting substrateis done by either; calendaring or pressing.

15. The method as claimed in any of the previous claims, wherein the transition metal salt solution is substituted with metalloid salt solutionof any metalloid in the periodic tablewhich includes, but is not limited to antimony, tellurium and germanium.